Drop-Size Distributions in Thunderstorms Measured by Optical Disdrometers during VORTEX2

KATJA FRIEDRICH AND EVAN A. KALINA

University of Colorado, Boulder, Colorado

FORREST J. MASTERS AND CARLOS R. LOPEZ

University of Florida, Gainesville, Florida

(Manuscript received 13 April 2012, in final form 22 October 2012)

ABSTRACT

When studying the influence of microphysics on the near-surface buoyancy tendency in convective thunderstorms, in situ measurements of microphysics near the surface are essential and those are currently not provided by most weather radars. In this study, the deployment of mobile microphysical probes in convective thunderstorms during the second Verification of the Origins of Rotation in Tornadoes Experiment (VORTEX2) is examined. Microphysical probes consist of an optical Ott Particle Size and Velocity (PARSIVEL) disdrometer that measures particle size and fall velocity distributions and a surface observation station that measures wind, temperature, and humidity. The mobile probe deployment allows for targeted observations within various areas of the storm and coordinated observations with ground-based mobile radars. Quality control schemes necessary for providing reliable observations in severe environments with strong winds and high rainfall rates and particle discrimination schemes for distinguishing between hail, rain, and graupel are discussed. It is demonstrated how raindrop-size distributions for selected cases can be applied to study size-sorting and microphysical processes. The study revealed that the raindrop-size distribution changes rapidly in time and space in convective thunderstorms. Graupel, hailstones, and large raindrops were primarily observed close to the updraft region of thunderstorms in the forward- and rear-flank downdrafts and in the reflectivity hook appendage. Close to the updraft, large raindrops were usually accompanied by an increase in small-sized raindrops, which mainly occurred when the wind speed and standard deviation of the wind speed increased. This increase in small drops could be an indicator of raindrop breakup.

1. Introduction

With the growing number of polarimetric Doppler weather radars, many studies have provided detailed observations of wind, hydrometeor type and distribution, and radar reflectivity within supercell thunderstorms (e.g., Bringi et al. 1991, 1996; Smyth and Illingworth 1998; Kennedy and Rutledge 1995; Hubbert et al. 1998; Wurman and Gill 2000; Burgess et al. 2002; Ryzhkov et al. 2005; Bluestein et al. 2007; Kumjian and Ryzhkov 2008, 2009; Romine et al. 2008; Van Den Broeke et al. 2008). While polarimetric radar observations can provide information related to the microphysical character of thunderstorms, the microphysics of the near-surface environment, believed to be most important for tornadogenesis, is usually below the radar horizon of even mobile polarimetric radar platforms. Several studies have shown that microphysics can play a key role in changing the thermodynamic structure of convective storms (Lord et al. 1984; Fovell and Ogura 1988; Liu et al. 1997; Dudhia 1989; McCumber et al. 1991; Ferrier et al. 1995; Gilmore et al. 2004; Morrison et al. 2009), which may modulate the near-surface buoyancy tendency and the likelihood of tornado development (Markowski et al. 2002; Shabbott and Markowski 2006; Grzych et al. 2007; Markowski et al. 2012). As such, in situ measurements of near-surface microphysics within precipitating downdrafts are needed to determine precipitation particle size distributions and to infer relations with polarimetric radar observations collected above the surface.

In this study, we discuss the deployment of a unique network of mobile and rapidly deployable low-cost laser

Corresponding author address: Dr. Katja Friedrich, ATOC, University of Colorado, UCB 311, Boulder, CO 80309-0311.
E-mail: katja.friedrich@colorado.edu

DOI: 10.1175/MWR-D-12-00116.1

disdrometers for the collection of in situ microphysical data within severe thunderstorms during the second Verification of the Origins of Tornadoes Experiment (VORTEX2; Wurman et al. 2012). To our knowledge, this study is the first time these instruments have been deployed in this manner. The mobile microphysical probe deployment coordinated with mobile polarimetric Doppler radars is a novel in situ microphysical data collection method within severe storms. In this study, we demonstrate that with a rigorous quality control scheme and a particle discrimination scheme, reliable observations of particle-size distributions (PSDs) in strong winds and heavy rainfall can be obtained, which can be used in the future to study microphysical processes and verify numerical models. To quantify the usefulness of mobile wind and disdrometer observations, the evolution of PSDs in two tornadic supercell thunderstorms and two merging convective storms that later produced a tornadic supercell thunderstorm is discussed and results are related to size-sorting theory and microphysical processes. This paper provides an observational context and information on the in situ microphysical data collection that complements associated modeling and physical analysis studies that examine the role of near-surface microphysics on the near-surface buoyancy tendency.

In situ microphysical observations in supercell thunderstorms that would support dual-polarization observations and fill in the gaps insufficiently covered by the radars are sparse. Measurements of PSD and fall velocity distribution largely originate from aircraft-mounted instruments (e.g., Musil et al. 1973; Brandes et al. 1995; Loney et al. 2002; Schlatter 2003) and ground-based disdrometers (Schuur et al. 2001; Bringi et al. 2003; Zhang et al. 2003; Cao et al. 2008; Thurai et al. 2010a,b). Schuur et al. (2001) provided one of the first studies analyzing raindrop-size distributions (DSDs) in supercell thunderstorms. Large rainfall rates and significant variability in the DSD were observed within the thunderstorm that were accompanied by many large particles with diameter $d > 5$ mm but also by a large concentration of small particles ($d < 1$ mm). Schuur et al. (2001) concluded that DSDs containing large particles ($d > 4$ mm) do not follow the generally used exponential Marshall–Palmer or gamma distributions, which has a major impact on the accuracy of radar-based estimates of rainfall rate in these environments. DSDs in convective rain in different climate regions were investigated by Bringi et al. (2003) and Thurai et al. (2010a). The authors distinguished between ''maritime like'' clusters of rain that were characterized by large concentrations of small drops and ''continental like'' clusters with a small concentration of large drops that were formed from the melting of graupel and tiny hailstones. Variations between maritime- and continental-like DSDs observed within a thunderstorm were also reported by Thurai et al. (2010b) using a 2D video disdrometer during a cool-season severe thunderstorm in Huntsville, Alabama, during January 2010. This thunderstorm produced a tornado rated as EF2 based on the enhanced Fujita (EF) tornado damage scale.

To quantify the surface microphysics in convective storms and complement the mobile radar observations during 12 weeks of the VORTEX2 field campaign (11 May–14 June 2009 and 3 May–14 June 2010), up to eight portable microphysical probes were deployed within 36 storms, which resulted in over 80 PSD transects through convective thunderstorms. Section 2 provides an overview of the instruments and deployment strategies. Section 3 describes the analysis techniques, including quality control and the discrimination between rain, graupel, and hail. In section 4 we will present DSD time series data for three selected cases with a further discussion on size-sorting theory and microphysical processes in section 5. Results are summarized in section 6.

2. Instruments and deployment strategies

a. *Microphysical probes and their use during VORTEX2*

The microphysical probes deployed during VORTEX2 consisted of the Ott Particle Size and Velocity (PARSIVEL) optical disdrometer and surface observation stations that recorded temperature, relative humidity, pressure, and wind from a propeller and/or sonic anemometer (Fig. 1). For applications within a severe storm environment, the small, lightweight, and inexpensive PARSIVEL disdrometers have enabled a portable, low-cost solution to collecting PSD measurements while yielding comparable data to video and impact disdrometer measurements in limited experiments (Tokay et al. 2001; Caracciolo et al. 2006; Krajewski et al. 2006; Battaglia et al. 2010; Thurai et al. 2011). The PARSIVEL uses a laser diode that produces a horizontal sheet of light 30 mm wide and 180 mm long (for more instrument information, see Loeffler-Mang and Joss 2000; Loeffler-Mang and Blahak 2001). Particles passing through the horizontal sampling area are sorted into particle-size (velocity) classes ranging between 0.312 and 24.5 mm (0.05 and 20 m s^{-1}) (Table A1 in Yuter et al. 2006). The sampling interval was set to 60 s in 2009 and 10 s in 2010. The calculations of DSD parameters derived from the moments of the DSD and the gamma functional fit are described in the appendix.

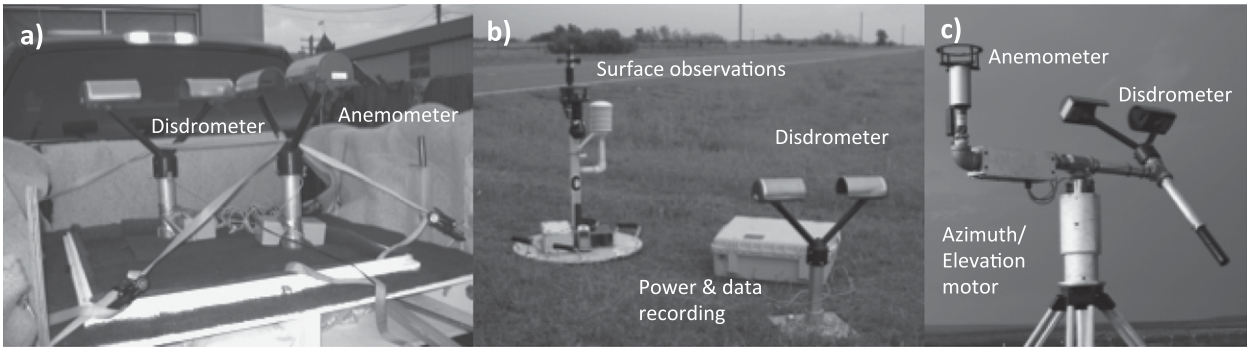

FIG. 1. Microphysical probe deployments in 2009 and 2010 during VORTEX2: (a) probes deployed in the back of a pickup truck in 2009, (b) unmanned stationary probe deployed in 2009 and 2010, and (c) articulating probe deployed in 2010. Microphysical probes consisted of PARSIVEL disdrometers and surface observation stations.

Although the robustness of the PARSIVEL disdrometers makes them a good choice for thunderstorm deployments, there have been considerable uncertainties during strong winds exceeding 10–20 m s^{-1} (Friedrich et al. 2012, manuscript submitted to *J. Atmos. Oceanic Technol.*, hereafter FHML). To improve the measurement accuracy in strong winds, several studies have suggested aligning the disdrometer sample area perpendicular to the wind direction (Bradley and Stow 1975; Griffiths 1975). The University of Florida (UF) designed an ''articulating'' disdrometer system that continuously aligns the disdrometer sample area with the mean 10-s particle trajectory, such that the measurement plane is perpendicular to the particle motion in an averaged sense (Lopez et al. 2011; Fig. 1c). A PARSIVEL disdrometer and an RM Young model 85106 2D sonic anemometer are mounted on an actively controlled platform that continuously changes the azimuthal and elevation angles of the disdrometer to orient the sample area semi-perpendicular to the particle motion. The azimuthal setpoint corresponds to the 10-s moving average of the wind direction. The elevation angle setpoint corresponds to the inverse arctangent of the 10-s moving average of the horizontal wind speed and the mean particle fall velocity; a particle fall velocity of 4.5 m s^{-1} ($d = 1.2$ mm) was assumed for the articulating disdrometer. A comparison between the stationary and articulating disdrometers deployed in five thunderstorms (~2 h) during VORTEX2 shows an agreement in reflectivity with median and spread differences (articulating–stationary) of −1.2 dB and 8 dB (Fig. 2). Spread is defined as the difference between the 16th and 84th percentiles. During strong wind conditions, the stationary disdrometer can occasionally measure ambiguous drop concentrations with large number concentration of raindrops with large diameters (>5 mm) and unrealistically low fall velocities (<1 m s^{-1}), while the ambiguous drop concentrations were never observed by the articulating disdrometer. For a more detailed discussion on stationary and articulating disdrometer measurements in strong winds, the authors refer to FHML. Note that in the comparison (Fig. 2) and the following analysis, time steps were completely eliminated when ambiguous drop concentrations were observed by the stationary disdrometer.

b. Deployment strategies of microphysical probes

In the first year of VORTEX2 in 2009, two microphysical probe systems operated by the University of Colorado (CU; denoted as CU01 and CU02 hereafter) were deployed. The equipment was secured to the bed of a pickup truck to facilitate rapid deployment in severe thunderstorms. The probes were operated in the bed of the pickup truck, which was parked (Fig. 1a). The truck deployment is very well suited for deployments of one to two disdrometers in less severe thunderstorms and allows for rapid redeployments. Measurement accuracy might be influenced by the truck itself through blockages by the driver's cabin (i.e., undersampling of particles) and splashing from the truck surfaces (i.e., increased number of smaller drops). Alternatively, the probes were also operated in an unmanned portable setup for deployments in severe environments (Fig. 1b). The unmanned system comprised a PARSIVEL disdrometer, an internal power supply, a data acquisition system, and a meteorological surface station. In the second year of VORTEX2 in 2010, a total of eight disdrometers were deployed: two from the University of Colorado (CU01 and CU02) and six from the University of Florida (denoted as UF01, UF03, UF04, UF05, UF06, and UF07 hereafter). With eight instruments, the truck deployments were no longer an efficient strategy. Therefore, all instruments were deployed on the ground (Figs. 1b and 1c). In 2010, disdrometers with horizontally oriented sample areas (denoted as stationary

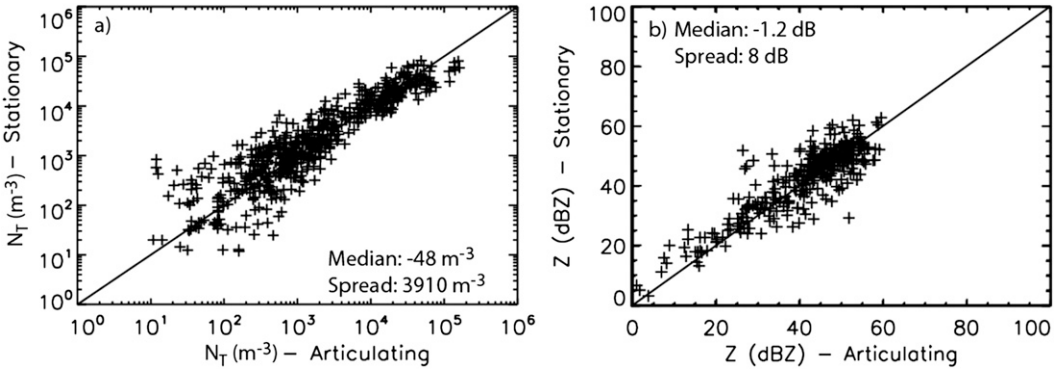

FIG. 2. Comparison between articulating and stationary disdrometer showing (a) N_T and (b) Z for $N_T > 1000$ m^{-3} for collocated measurements on 2 Jun (UF01, UF06), 7 Jun (UF01, UF07), 9 Jun (UF01, UF05 and UF03, UF06), and 10 Jun 2010 (UF03, UF06).

disdrometers CU01, CU02, UF03, UF04, UF05, UF06, and UF07) and articulating disdrometers (UF01 and UF03) were used. The analysis shown hereafter (section 4) includes data from both the articulating and stationary disdrometers that were deployed during 2010. Data from 2009 and the truck deployments are not shown in this paper because most of the sampled thunderstorms were not severe and in the few severe thunderstorms the deployment locations of the two disdrometers did not meet our objectives as described in the following paragraph.

The objectives of the portable microphysical probe deployments during VORTEX2 were to observe temporal and spatial variations in PSDs by transecting supercell thunderstorms within the range of the mobile radar platforms (<25 km) and to repeat this process several times to document the temporal variation in the PSD. To achieve this goal, probes were positioned several minutes in advance of the thunderstorms on the south side of the forward-flank downdraft (FFD) using a picket fence strategy with relatively close spacing of 0.5–1 km (Fig. 3). After the storm passed over the instruments, the microphysical probes were relocated ahead of the storm and the measurements were repeated. The deployment sites were carefully chosen to minimize effects of splashing from surrounding obstacles such as cars passing the instruments at close distance or vegetation in the instruments' vicinity. The effects of drops hitting the instrument surfaces and splashing into the sample volume will be discussed in section 3b. Additionally, instruments were leveled with respect to the ground by using fixed levels that were attached to the instruments and tripods with levels to account for unevenness of the ground. Anemometers were aligned to magnetic north using built-in compasses.

3. Methods

a. *Fall velocity correction for articulating disdrometers*

The alignment of the sample area perpendicular to the wind results in a measured particle velocity, which is composed of the wind speed and the particle fall velocity (also referred to as the fall velocity hereafter) as indicated in the schematic in Fig. 4a. Azimuth and elevation angles of the rotating motors together with the wind vector are recorded at a frequency of 17 Hz and averaged over 10 s to complement the time resolution of the PARSIVEL measurements. The wind information is used to derive the particle fall velocity v_{tc}:

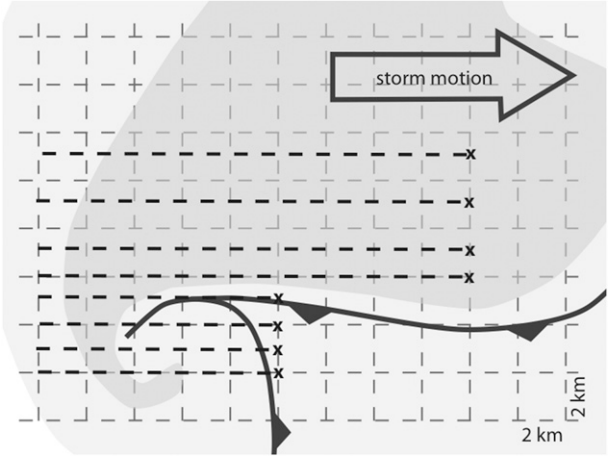

FIG. 3. Schematic of the microphysical probe deployment strategy. Deployment locations are depicted by the black ×s. Black, dashed lines represent transects made by each instrument through the storm. Probes were deployed ahead of the storm and picked up after the storm passed over the instruments. The road network is indicated by gray, dashed lines. The light gray shading represents the radar echo. Frontal symbols denote the gust front.

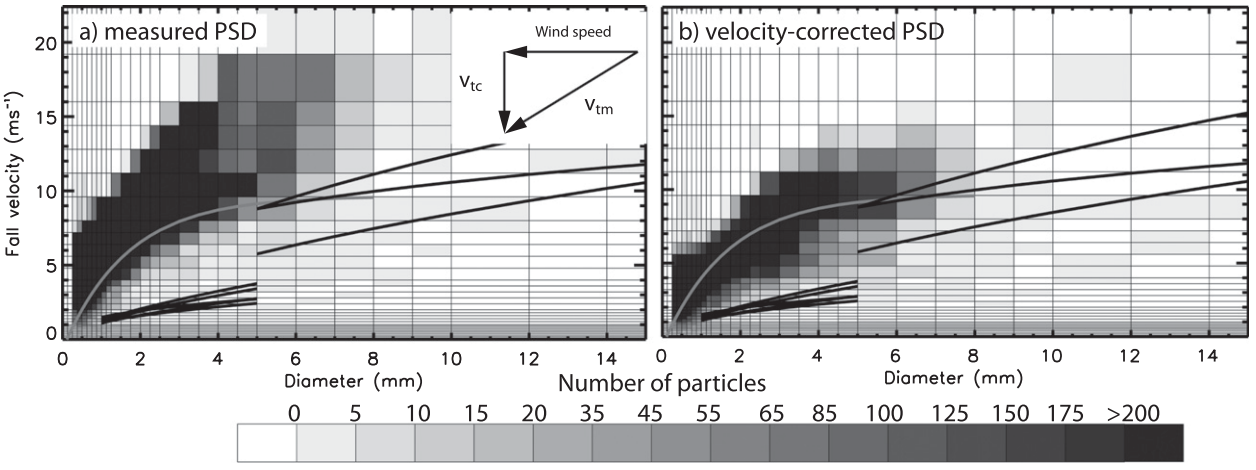

FIG. 4. Velocity–diameter histograms observed on 12 Jun 2010 by the articulating disdrometer UF01: (a) particle-size distribution measured in the articulating mode with the measured fall velocity v_{tm} and (b) particle-size distribution after fall velocity was corrected for wind speed indicating the corrected fall velocity v_{tc}. Solid lines indicate the empirical fall velocity–diameter relationships for hail, graupel, and rain (see Table 1 and Fig. 5a).

$$v_{tc} = v_{tm} \cos\left[\tan^{-1}\left(\frac{\sqrt{u^2 + v^2}}{4.5\,\mathrm{m\ s^{-1}}}\right)\right], \qquad (1)$$

where v_{tm} represents the particle velocity measured by the articulating disdrometers and u and v the west–east and south–north wind components, respectively. Note that the azimuthal and elevation control software was programmed to assume a constant particle fall velocity of 4.5 m s^{-1} for the articulating disdrometers (section 2a). Figure 4 shows a fall velocity–diameter histogram with PSD accumulated over 10 s from the articulating disdrometer, before and after the fall velocity correction was applied.

b. *Quality control for articulating and stationary disdrometers*

The quality control procedure addresses three main error sources related to measurement inaccuracies: (i) strong winds leading to a misclassification of particles, (ii) particles falling through the edges of the sample area, and (iii) splashing effects from particles hitting instrument surfaces, breaking up into smaller particles, and then passing through the sampling area (e.g., Sevruk 1982; Illingworth and Stevens 1987; Nespor et al. 2000; Schuur et al. 2001; Yuter et al. 2006; FHML). All of these effects result in spurious particles with unrealistic fall velocities and diameters compared to values typically observed for rain, graupel, and hail.

Due to the measurement principle, which is based on the magnitude and duration of the laser light attenuation described in section 2a, the stationary PARSIVEL disdrometer measurements in strong wind with speeds >10 m s^{-1} are prone to the misclassification of particles (FHML). This misclassification is characterized by a large number concentration of raindrops with large diameters (>5 mm) and unrealistically slow fall velocities [<(1–2) m s^{-1}; hatched area in Fig. 5a denoted as strong wind effects]. The misclassification is consistently observed by stationary disdrometers but is not observed by articulating disdrometers, which continuously orient the sample area perpendicular to the wind (FHML). To address this misclassification in the VORTEX2 data, the time step was completely removed from the analysis when large ($d > 5$ mm), slow-falling ($v < 1$ m s^{-1}) particles were observed (FHML).

For those time steps that were not affected by strong winds, particles most likely related to splashing and margin faller effects have been removed (hatched areas in Fig. 5a denoted as splashing and margin fallers, respectively). If particles fall through the edges of the sample area, they appear as small particles that move faster than the empirical fall velocity–diameter relation for rain, graupel, and hail suggests. To avoid misinterpretation of margin fallers being fully resolved raindrops, a quality control procedure is applied to the raw measurements that filter particles that have a diameter less than 8 mm and have fall velocities that are 60% larger than the fall velocity–diameter relationship for rain as indicated in Fig. 5a. Jaffrain and Berne (2011) compared 15 months of rain gauge and PARSIVEL disdrometer measurements and concluded that excluding data that are more than 60% above or below the fall velocity–diameter relationship for rain will give a good level of agreement (3.5% differences of total rain amount) between PARSIVEL disdrometers and rain gauges. Other

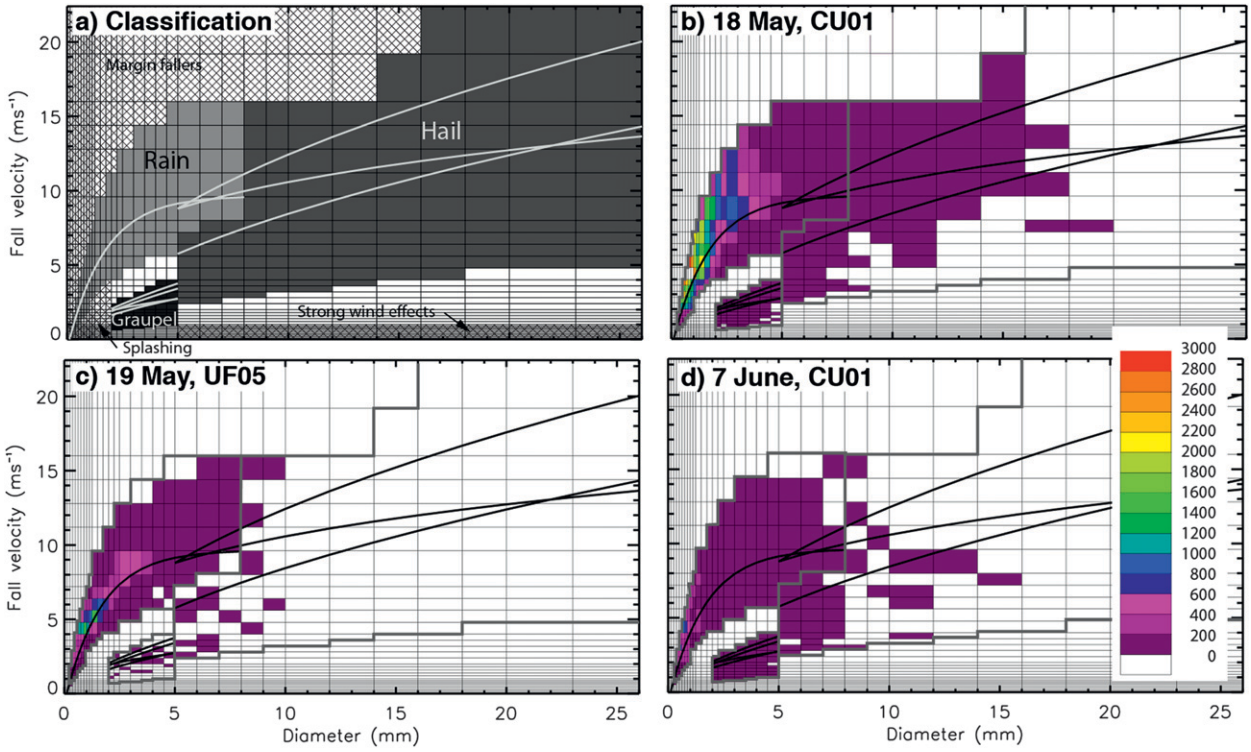

FIG. 5. (a) Particle classification scheme based on typical diameter ranges and fall velocity–diameter relationships for rain (medium gray shading), hail (dark gray shading), and graupel (black shading). Light gray lines indicate fall velocity–diameter relationships for rain, graupel, and hail, respectively. More information is provided in section 3c and Table 1. Accumulated number concentrations (raw counts in color) for selected instruments for the entire measurement period on (b) 18 May, (c) 19 May, and (d) 7 Jun 2010. In (b)–(d) the particle classification scheme is provided by the light gray lines; fall velocity–diameter relationships are indicated in black. Particle counts outside the classification ranges [white and hatched areas in (a) have been removed in (b)–(d).]

studies use a threshold of 40% above or below the fall velocity–diameter relationship for rain to remove misclassified drops (Kruger and Krajewski 2002; Thurai and Bringi 2005).

A further error source is related to splashing, which causes drops to hit the instrument surfaces, break apart, and rebound back into the sample area. Splashing effects are usually observed in the smallest size classes ($d < 2$ mm) with a wide range of fall velocities between 0.5 and 9 m s^{-1} (Barthazy et al. 2004; Krajewski et al. 2006; Yuter et al. 2006). Here, the raindrops, most likely related to splashing, are filtered by removing particles that have a diameter <2 mm and fall velocities 60% smaller than the fall velocity–diameter relationship for rain (Fig. 5a).

c. *Discrimination between graupel, hailstones, and rain for stationary and articulating disdrometers*

To calculate the moments of the raindrop size distribution (i.e., reflectivity Z, rainfall rate R, liquid water content w, and median-volume diameter D_0) and the parameters of the gamma functional fit for raindrops (intercept parameter N_0, slope parameter Λ, and shape parameter μ), we need to distinguish between ice particles and raindrops. The calculation of the moments of the DSD and gamma functional fit are described in the appendix, while the following section focuses on using typical diameter ranges and fall velocity–diameter relationships listed in Table 1 to distinguish between graupel, hail, and rain (Fig. 5a and Table 1). Raindrops should have diameters of <8 mm (Rauber et al. 1991; Kobayashi and Adachi 2001; Szumowski et al. 1998). Graupel particles should have diameters less than 3–4 mm (Locatelli and Hobbs 1974). To distinguish between small raindrops and hail, we chose a diameter range between 2 and 5 mm for graupel. The 2-mm threshold was chosen to better distinguish between graupel and splashing raindrops, which should have fall velocity and diameter characteristics that are similar to small graupel. Particles classified as hail must have diameters that exceed 5 mm (Huschke 1959). Note that the 5-mm threshold is an arbitrary threshold that we use to distinguish between small hail or graupel and larger hailstones. As shown in Figs. 5b–d, the amount and size of

TABLE 1. Diameter range and fall velocity–diameter relationships used for the discrimination between rain (Gunn and Kinzer 1949, GK49; Atlas et al. 1973, A73), graupel (Locatelli and Hobbs 1974, LH74), and hail (Knight 1983, K83).

Category	Diameter range (mm)	Fall velocity (v in m s^{-1})–diameter (d in mm) relationships	Reference
Rain	$d < 8$	$v = (9.65–10.3)^{(-0.6d)}$	GK49, A73
Graupel	$2 \le d \le 5$	Lump graupel: $v = 1.3d^{0.66}$, $v = 1.5d^{0.37}$	LH74
		Conical graupel: $v = 1.2d^{0.65}$	LH74
		Hexagonal graupel: $v = 1.1d^{0.57}$	LH74
Hail	$d > 5$	Low-density hailstones [$\rho \sim$ (0.31–0.61) g cm^{-3}]: $v = 8.445(0.1d)^{0.553}$, $v = 12.43(0.1d)^{0.5}$	K83
		Higher-density hailstones ($\rho \sim 0.82$ g cm^{-3}): $v = 10.58(0.1d)^{0.267}$	K83

small and larger ice particles can strongly vary between the cases. For instance, on 18 May, large amounts of small and large ice particles were observed while on 19 May the diameter of the ice particles was <10 mm and fewer ice particles were observed compared to 18 May. On 7 June a large number of smaller ice particles were observed with a few examples of larger hail. To reduce the possibility of large raindrops [$d \sim$ (5–8) mm] being categorized as hail, all large particles between $d \sim$ (5–8) mm that are within ±60% of the fall velocity–diameter relationship are classified as rain. Note that this can cause some misclassifications in particular in the presence of low-density small hailstones combined with large raindrops.

In a second step, fall velocity–diameter relationships are used to distinguish graupel from rain and hail from large raindrops. While raindrops have a relatively well-defined fall velocity–diameter relationship, the various shapes of graupel and hail result in a large variety of fall velocity–diameter relationships, as summarized in Table 1. For the lower graupel and hail thresholds, we chose the minimum fall velocity values for each diameter bin from the various relationships listed in Table 1, respectively, and applied the 60% tolerance interval. For the upper graupel class threshold, we choose the maximum fall velocity value for each diameter bin from the fall velocity–diameter relationships for graupel. This approach reduces the possibility that spurious raindrops and splashing raindrops are classified as graupel. For the upper hail class threshold, the margin faller thresholds were extended to 16 mm, as shown in Fig. 5. To distinguish between large raindrops and small hail with diameters ranging between 5 and 8 mm, the average between the fall velocity–diameter relationship for rain and the fall velocity–diameter relationship for hailstones (Knight 1983) is used.

Due to the sparse distribution of hail and graupel and the small measurement area of the disdrometer, the instrument is not capable of reproducing a representative particle size distribution for hail and graupel. Therefore, only raindrop-size distributions are analyzed in this paper. Time periods when graupel and hail were observed are highlighted. However, the latter does not indicate how many or what size graupel or hail particles were observed during the time period (cf. Figs. 5b and 6c).

4. Drop-size distributions for selected cases

a. Isolated tornadic supercell thunderstorm

One microphysical probe (stationary disdrometer CU01) was deployed on 18 May 2010 near Dumas, Texas, ahead of an isolated right-moving supercell thunderstorm (Figs. 6 and 7). The Weather Surveillance Radar-1988 Doppler (WSR-88D) and the Doppler on Wheels (DOW; Wurman et al. 2007, 2010, 2012) radar reflectivity Z results as well as winds observed at the instrument site (Figs. 6a,b and 7) indicate the location of the instruments with respect to the supercell thunderstorm. We can estimate that the instrument intercepted the southern side of the forward-flank downdraft (FFD) between about 2300 and 2340 UTC when WSR-88D $Z > 60$ dBZ and winds were <6 m s^{-1} with an easterly or northeasterly component. The southern side of the precipitation core of the storm (i.e., area of highest reflectivity) was intercepted between 2340 and 0000 UTC with WSR-88D $Z >$ 60 dBZ and winds > 6 m s^{-1} from the north and northeast, while the rear-flank downdraft (RFD) passed the instruments after ~0000 UTC. A tornado vortex signature in the Doppler velocity with a change in velocity of ~58 m s^{-1} over a distance of 0.3 km about 50 m above the surface was observed at 2328 UTC for 1 min by the mobile Doppler on Wheels radar (Fig. 7a; Wurman et al. 2007, 2010).

A few hail and graupel particles and mainly raindrops with low (<50 mm^{-1} m^{-3}) and medium (50–1000 mm^{-1} m^{-3}) number concentrations of small- ($d < 2$ mm) and medium-sized [$d \sim$ (2–4) mm] particles, respectively, were observed in the FFD as the storm approached the instrument between 2300 and 2330 UTC

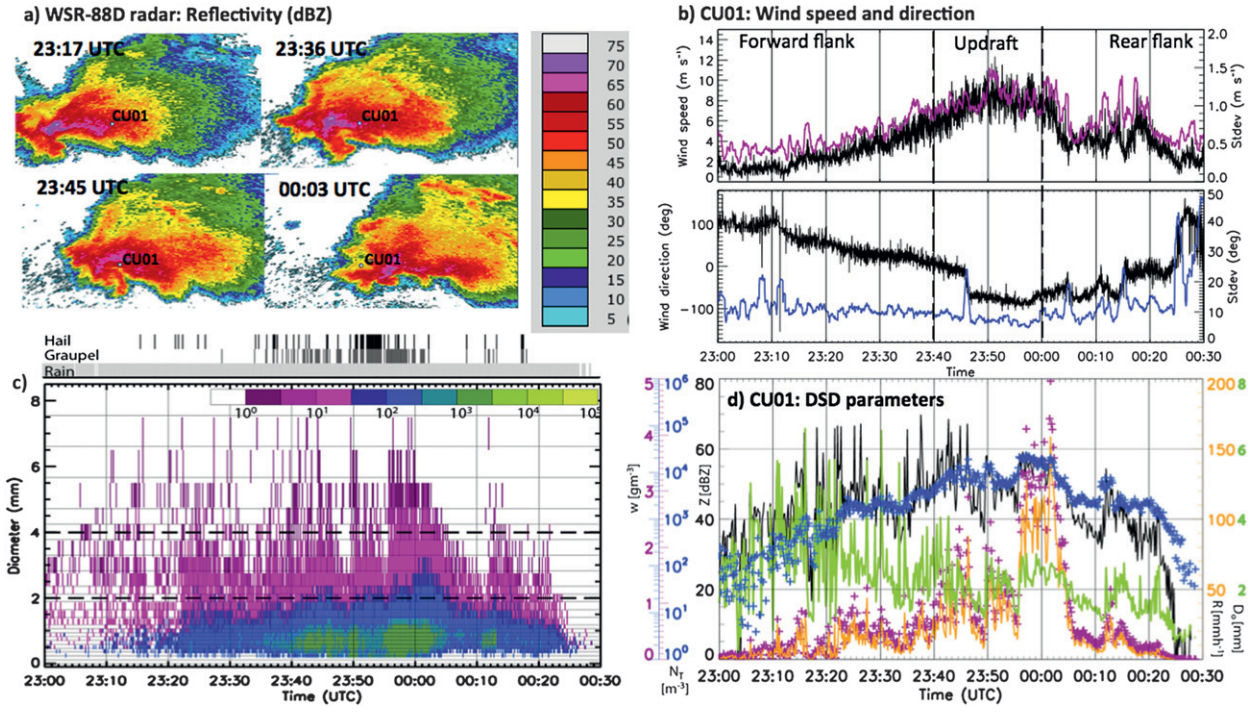

FIG. 6. Measurements of the 18 May 2010 case in Dumas, TX: (a) WSR-88D radar reflectivity (dBZ) at 0.5°-elevation angle from Amarillo, TX (KAMA), for selected times between 2317 and 0003 UTC. The distance between the storm and the radar was ~76 km, i.e., the radar beam was ~1 km above ground level. The location of the stationary disdrometer CU01 is plotted. (b) Wind speed (top panel, black line, m s^{-1}), wind direction (bottom panel, black line, °), and standard deviation of wind speed (top panel, purple line) and direction (bottom panel, blue line). The anemometer was deployed at the location of CU01. (c) Time series of quality controlled number concentrations per unit volume for particles classified as rain (color-coded scale at the top) as a function of diameter class and time measured by the microphysical probe CU01. Number concentrations are plotted every 10 s. Diameter bins are indicated by solid black lines, and 2- and 4-mm diameters are denoted by thick dashed lines. Times when rain, graupel, or hail were observed are indicated on the top. (d) Time series of disdrometer-derived DSD parameters for rain: R, orange line; w, purple + signs; Z, black line; D_0, green line; and N_T, blue + signs. The approximate transition between FFD, the main storm updraft, and RFD are indicated in (b).

(Fig. 6c). Between this time period, the disdrometer-based Z ranged on average from 20 to 60 dBZ, while the rainfall rate R and the liquid water content w increased to 40 mm h^{-1} and 1 g m^{-3}, respectively (Fig. 6d). The total number concentration N_T was relatively small (<5000 m^{-3}) and the median-volume diameter D_0 varied strongly between 2 and 6 mm. The DOW reflectivity indicates an increase in Z from mainly below 50 dBZ at 2320 UTC to isolated areas with $Z \sim$ (55–60) dBZ at 2338 UTC (Figs. 7a,b). Note that the DOW reflectivity was not corrected for radar beam attenuation caused by heavy rain and ice particles. The radar attenuation led to a sharp decrease in Z and a complete loss of the signal on the northern side of the storm.

When the storm continued to pass over the instrument between 2330 and 2350 UTC with the instruments getting closer to the updraft region (Figs. 7c,d), graupel was observed almost continuously and the number of times when hail was present increased (Fig. 6c). However, Fig. 5b shows that throughout the storm only a few ice particles (<200 particles over 90 min) with large, medium, and small sizes were observed. On the other hand, we can also not fully exclude the possibility that spuriously measured raindrops might have been classified as ice particles. When the instruments were picked up after the deployment, small graupel was still on the ground. Compared to earlier times, the number concentrations of large ($d > 4$ mm), medium-sized [$d \sim$(2–4) mm], and small ($d < 2$ mm) raindrops increased (Fig. 6c) after 2350 UTC, which is also reflected in an increase in the intercept parameter N_0 while the slope Λ and shape μ parameters of the DSD gamma fit remained flat (Fig. 8a; see the appendix). The WSR-88D reflectivity values reached a maximum at ~70 dBZ at 2345 UTC. Liquid water content and the total number concentration of particles also increased to 3 g m^{-3} and 10 000 m^{-3}, respectively. Based on the WSR-88D and DOW reflectivity data, the instrument intercepted an area of small reflectivity values between 2350 and 2355 UTC that was likely related to the proximity of

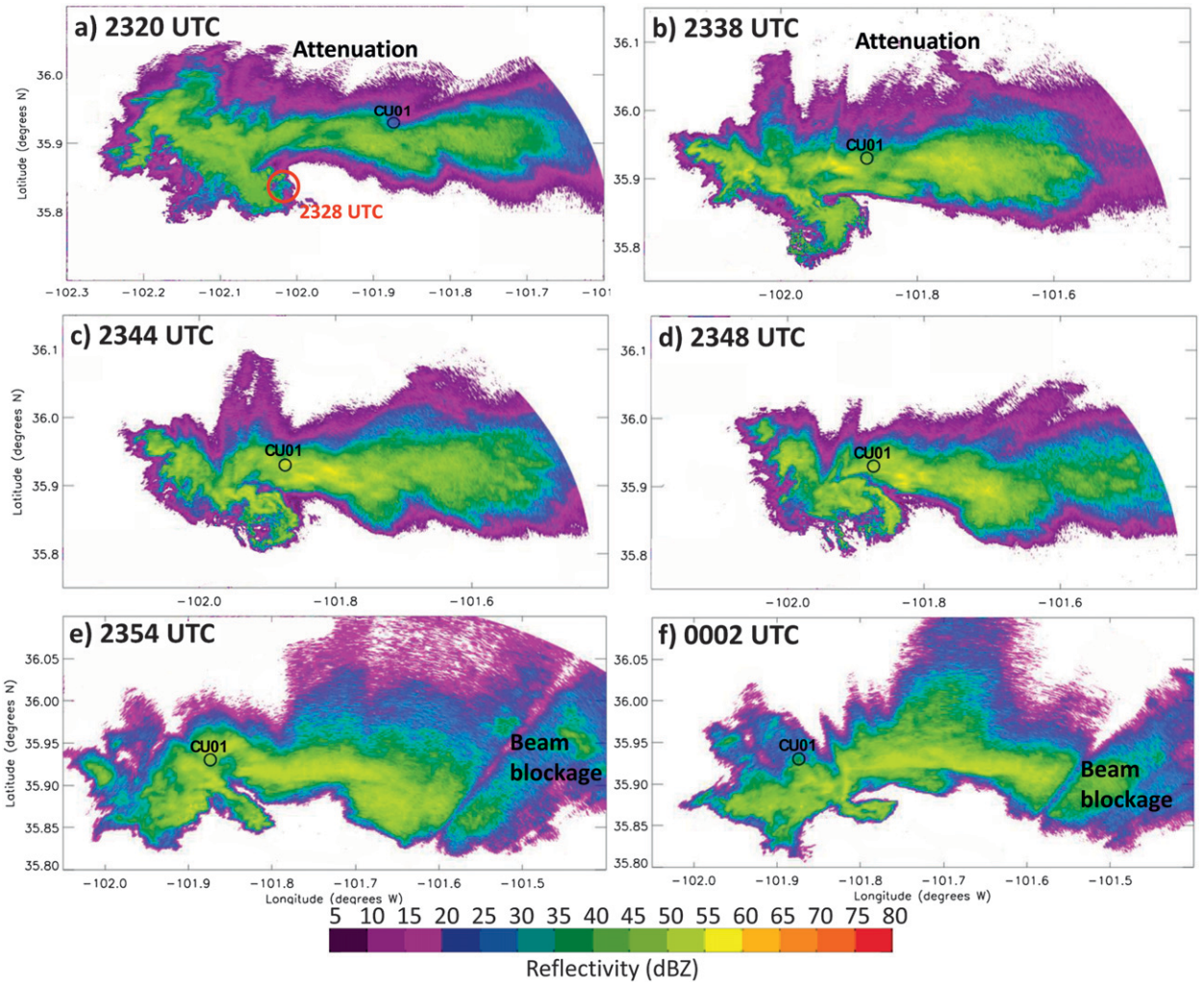

FIG. 7. DOW radar reflectivity observed at 1°-elevation angle by DOW7 on (a),(e) 18 May and on (f) 19 May 2010; and by DOW6 on (b)–(d) 18 May 2010. Disdrometer indicated by a black circle. Note the DOW reflectivity has not been corrected for attenuation of the radar beam by large raindrops and ice particles; i.e., reflectivity on the northern side is reduced at all times due to radar beam attenuation as indicated in (a),(b). Radar beam blockage due to obstacles on the ground occurs on the eastern side of the storm in (e),(f). The distance between the radar and the disdrometers ranges from 14 km in (b)–(d) to ~26 km in (a),(e),(f). A tornado vortex signature was observed by DOW6 at 2326 UTC; the location is indicated by the red circle in (a).

the updraft area. It is expected that hail shafts (i.e., small downdrafts containing large amounts of hail) occurred near the updraft (i.e., prior to 2350 UTC and after 2355 UTC), but not in the updraft region itself (2350–2355 UTC). Since the fall velocity of hail is much larger than that of rain or graupel, hailstones usually fall to the ground near the updraft and were almost continuously observed by the disdrometer around 2355 UTC (Fig. 6c). Note that since the PARSIVEL sampling area is limited to 180 mm × 30 mm, large hailstones cannot be fully resolved by the instrument on a consistent basis. Overall, the microphysical probes observed large-sized hailstones and raindrops, possibly related to melting ice particles, and large Z values in the areas close to the updraft. Interestingly, greater number concentrations (>1000 mm^{-1} m^{-3}) of smaller-sized ($d < 2$ mm) particles were observed between 2340 and 0005 UTC. The increase in the number of smaller drops is also reflected in the gamma functional fit, indicating an increase in slope, intercept, and shape parameters (Fig. 8a). The instrument intercepted an area of high rainfall rate around 0000 UTC before transitioning into the RFD (Figs. 7e,f). The largest values of R [~(70–150) mm h^{-1}] and w (2–5 g m^{-3}) were observed during that time, with disdrometer-based Z and D_0 values ranging around 50 dBZ and 2–3 mm, respectively. This area was characterized by large concentrations of small ($d < 2$ mm) and large ($d > 4$ mm) raindrops, graupel, and hailstones.

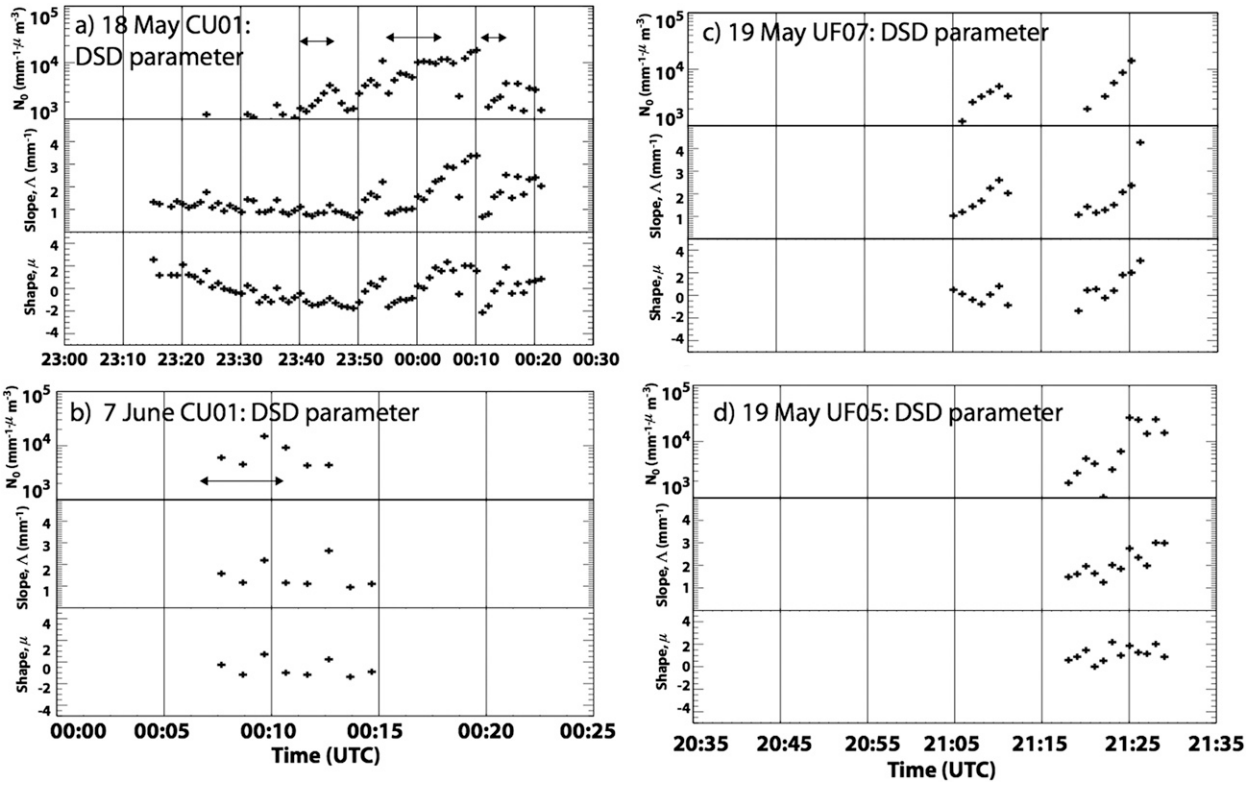

FIG. 8. Temporal evolution of intercept N_0, slope Λ, and shape μ parameters observed by (a) CU01 on 18 May, (b) CU01 on 7 Jun, (c) UF07 on 19 May, and (d) UF05 on 19 May 2010. Arrows indicate times discussed in the text.

Within a few minutes, a sharp decrease in the number concentrations of large and small particles was observed after 0002 UTC. While N_0 remained flat, μ and Λ increased (Fig. 8a). When the instrument sampled the edge of the storm after 0005 UTC, disdrometer-based Z and w dropped below 40 dBZ and <1 g m^{-3}, respectively. A few hailstones, and occasionally graupel, were observed. At the western edge of the storm, no large particles were observed, and the number concentrations of medium and small particles decreased with D_0 ranging between 1 and 2 mm.

b. Merging thunderstorms

Five microphysical probes were deployed between 2036 and 2136 UTC on 19 May 2010 near Kingfisher, Oklahoma, ahead of a supercell thunderstorm moving eastward (Figs. 9 and 10). At the beginning of the deployment (2036–2115 UTC), the target thunderstorm approached from the west and merged with a smaller, northward-moving convective cell that was located to its southeast (Figs. 9a and 10a–c). After the storms merged, the radar reflectivity intensified and the supercell thunderstorm strengthened. A newly formed cell south of the merged thunderstorm was observed at ~2114 UTC and also merged with the thunderstorm between 2118 and 2128 UTC (Figs. 10d–g). No tornado vortex signature in the Doppler velocity field was observed during the disdrometer deployment between 2026 and 2135 UTC by any of the mobile Doppler radars [i.e., DOWs and the National Oceanic and Atmospheric Administration's X-band, dual-Polarized radar (NOXP)]. However, this thunderstorm later developed a tornado vortex signature at ~2300 UTC with Doppler velocity differences of 52 m s^{-1} over a 0.5-km distance.

Figures 9b and 9c show the time series of DSD and DSD parameters. Based on the WSR-88D and NOXP radar data, the precipitation core of the southern convective cell passed over the microphysical probe UF07, while UF04 and UF05 measured the DSD at the edges of the southern convective cell prior to 2110 UTC (Figs. 9a and 10a–c). The edges of the storm and the convective cell were characterized by larger raindrops (UF07, $D_0 \sim$ 4 mm; UF04–UF05, $D_0 \sim 2$ mm) decreasing to small-sized raindrops with $D_0 \sim 1$ mm, when the storm moved over the instruments prior to 2110 UTC. The absence of large drops was associated with an increase in the slope parameter (Fig. 8c), while the increase in N_0 can be associated with an increase in small-size drops. UF04 and

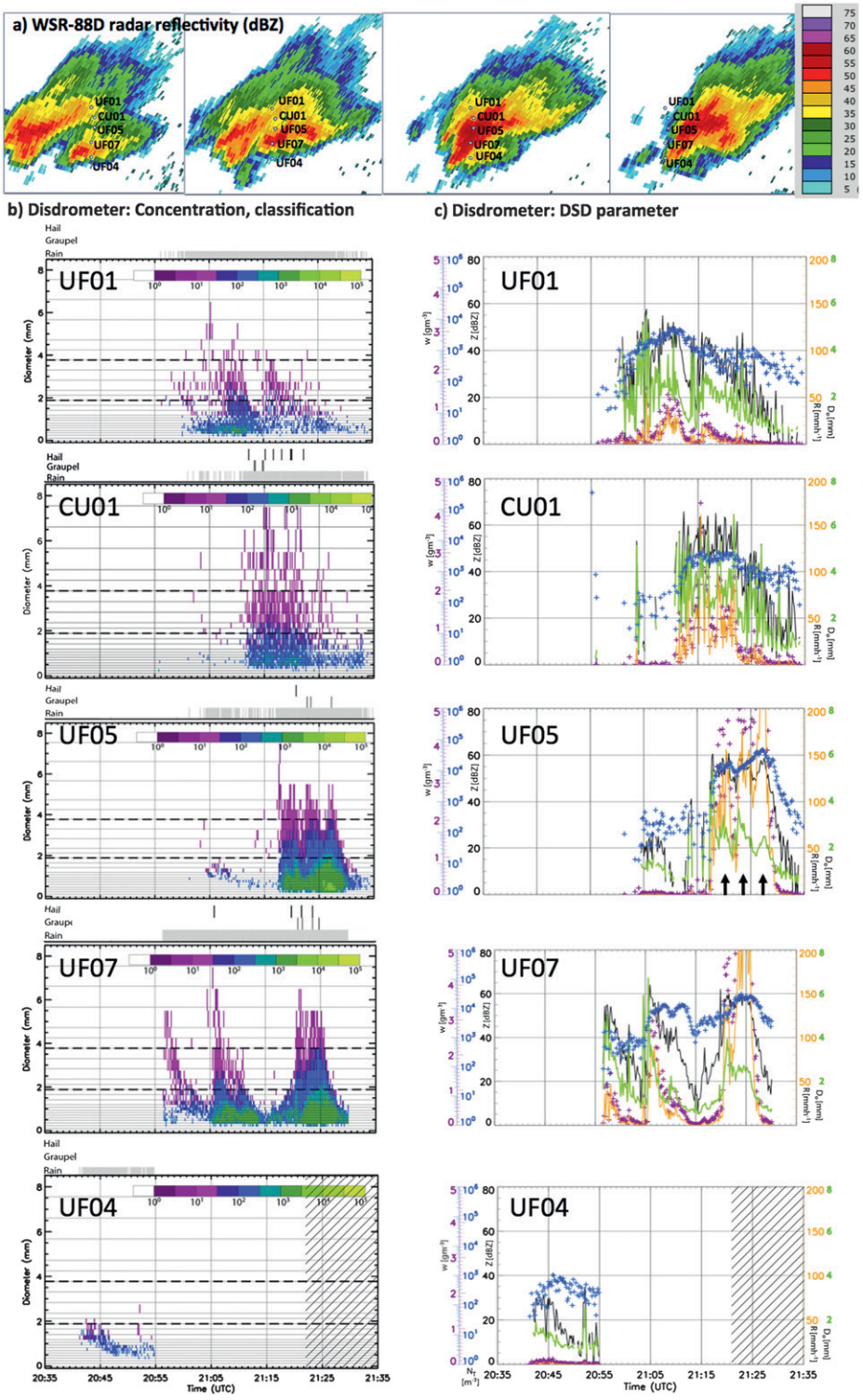

FIG. 9. As in Fig. 6, but for the deployment on 19 May 2010 near Kingfisher, OK. The articulating microphysical probe UF01 and the stationary probes CU01, UF05, UF07, and UF04 were deployed along a north–south road as depicted in (a). WSR-88D radar reflectivity (dBZ) from Oklahoma City, OK (KTLX), is also shown in (a). The distance between the radar and the storm was ~170 km; i.e., the radar beam was ~3.1 km above ground level. Black arrows in the UF05 panel indicate three reflectivity maxima that are discussed in the text. Note that the disdrometer UF04 was only deployed between 2035 and 2122 UTC; i.e., times with no measurements from UF04 are indicated as hatched areas.

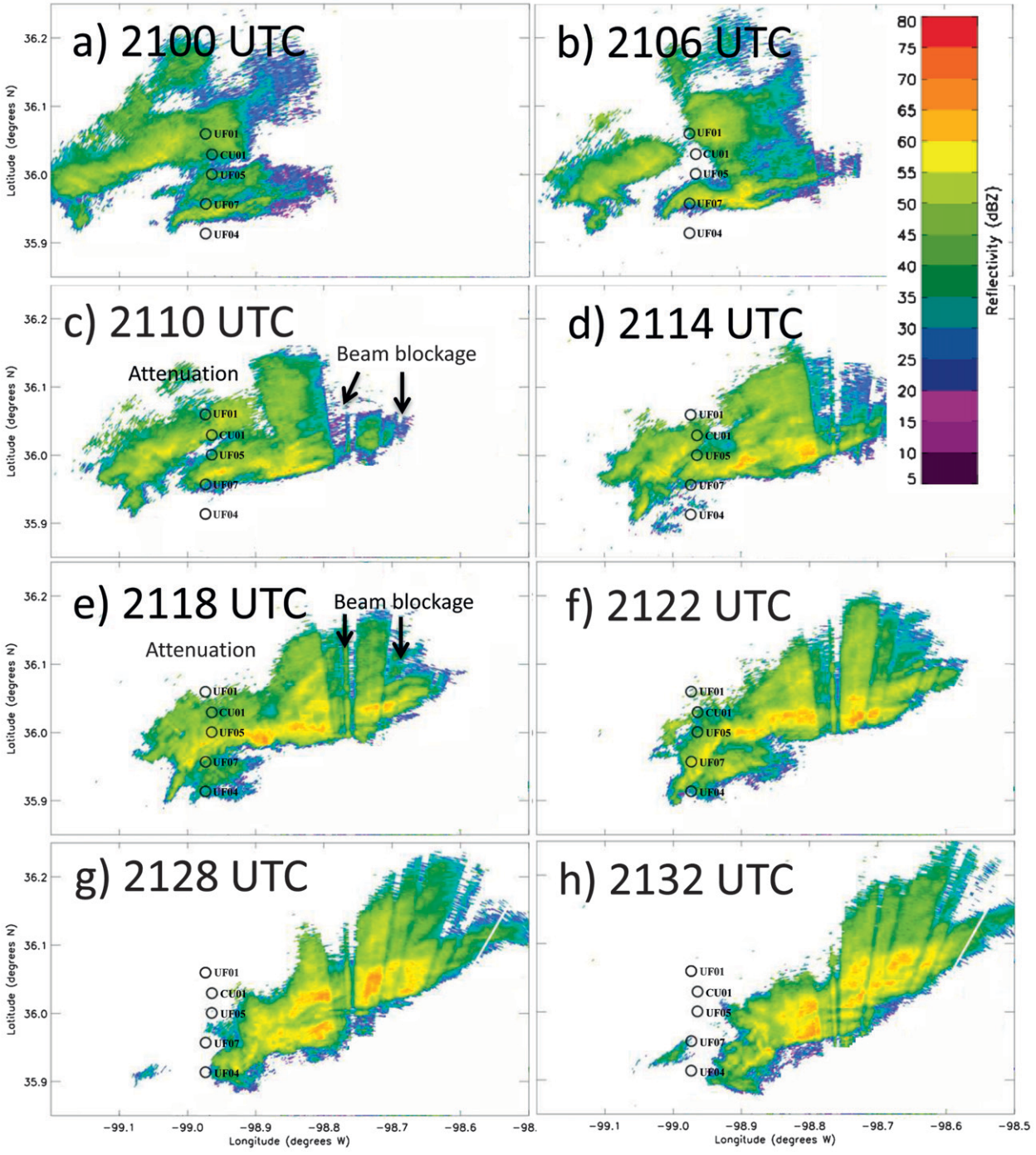

FIG. 10. Radar reflectivity (dBZ) at 1°-elevation angle observed on 19 May 2010 by the NOXP radar. The radar was located south of the storm about ~25 km from UF04. NOXP data were corrected for radar beam attenuation using the dual-polarization measurements. The radar beam was partially and completely attenuated at all times by ground clutter in the FFD region of the storm as indicated in (c) and (e). Note that in (a)–(f), the disdrometer UF04 was only deployed between 2035 and 2122 UTC.

UF05 observed mainly raindrops of <2-mm diameter ($D_0 \sim$ 1–2 mm, $w < 0.5$ g m^{-3}, disdrometer-based $Z <$ 30 dBZ), which decreased in diameter to <1 mm ($D_0 \sim$ 1 mm, $Z \sim$ 10 dBZ) between 2050 and 2055 UTC and 2110 an 2115 UTC, respectively. In contrast, UF07 first observed particles of 3–5 mm in diameter ($D_0 \sim$ 5 mm, $w \sim$ 1–1.5 g m^{-3}, $Z \sim$ 40–50 dBZ) between 2055 and 2100 UTC, which may have consisted of a mixture of

larger raindrops and tiny hailstones. After 2100 UTC, the particle sizes decreased to $d < 2$ mm ($D_0 \sim 1$ mm, $w < 0.5$ g m^{-3}, $Z < 30$ dBZ), before a second convective cell was intersected between 2105 and 2115 UTC. At this time, small-sized particles were observed during the entire 10 min, while large particles were only observed at ~2105 UTC.

After 2115 UTC, the rear portion of the merged thunderstorm intensified; that is, NOXP radar reflectivity increased to 65 dBZ (Figs. 10d–h). The microphysical probes transected the northern (UF01, CU01) and southern (UF07) parts of the merged storm as well as its precipitation core (UF05) and developing hook appendage (UF04). The DSDs from the south side and the precipitation core of the merged storm show a small number concentration (<50 mm^{-1} m^{-3}) of large ($d > 4$ mm) particles. Small amounts of graupel were mainly observed by the instruments closest to the precipitation core (CU01, UF05, and UF07). A moderate concentration (50–1000 mm^{-1} m^{-3}) of medium-sized [$d \sim$ (2–4) mm] and a large concentration (>1000 mm^{-1} m^{-3}) of small ($d < 2$ mm) particles were observed by UF05 and UF07 between 2115 and 2130 UTC. UF07 observed a decrease in D_0 from 5 to 1 mm with an increase in slope, shape, and intercept parameters (Fig. 8c) between 2105 and 2110 UTC and around 2125 UTC, while the number concentration remained the same. If the number concentration remains constant while the size of the raindrops decreases, evaporation due to the entrainment of dry air might be the cause. Since the storm on 19 May moved much faster (>30 kt) than the isolated supercell on 18 May, large temporal variability in the DSD was observed over only 10 min. During this time, the disdrometer-based reflectivity varied between 20 and 660 dBZ, w between 2 and 65 g m^{-3}, and D_0 between 2 and 6 mm. The DSDs deployed within the precipitation core region (UF05, 2118–2128 UTC; Figs. 8d and 10e–g) also showed a rapid change over a 3-min interval, with three maxima in reflectivity and diameter occurring at 2120, 2123, and 2127 UTC (black arrows in Fig. 9c; UF05), when D_0 peaked at 3.5 and 2.5 mm, respectively.

The northern sides of the FFD and RFD that were farther away from the precipitation core (UF01 and CU01; Figs. 9 and 10) contained a small concentration (<50 mm^{-1} m^{-3}) of medium-sized [$d \sim$ (2–4) mm] particles and a moderate concentration (<50 mm^{-1} m^{-3}) of small ($d < 2$ mm) particles. Particles with larger diameters ($d > 4$ mm) were only observed occasionally by CU01. Disdrometer-based reflectivity values were mainly around 30–60 dBZ and dropped to <30 dBZ close to the edge of the storm after 2125 UTC. No particles were observed by UF04 between 2055 and 2122 UTC. UF04 was replaced at 2122 UTC before it would have intersected the storm's hook appendage between 2120 and 2128 UTC (Figs. 10f,g). Since there is no indication of an instrument failure during the deployment between 2035 and 2122 UTC, it is likely that the particles observed by the NOXP radar with $Z < 35$ dBZ prior to 2122 UTC evaporated on their way to the ground (the height difference between the NOXP radar beam and UF04 was ~450 m). No precipitation was observed when the instruments were picked up at 2122 UTC.

c. *Hook appendage of supercell thunderstorm*

Three microphysical probes were deployed between 0000 and 0025 UTC on 7 June 2010 near Scottsbluff, Nebraska, ahead of the reflectivity hook-echo region (Figs. 11a and 12). The supercell thunderstorm moved rapidly (>30 kt) toward the east. A tornado vortex signature with a change in Doppler velocity of ~50 m s^{-1} over a distance of 1.3–2 km was observed near the ground (~150 m) between 0004 and 0007 UTC by the mobile Doppler radars. Based on the WSR-88D and DOW radar and the surface wind observations (Figs. 11–13), the tornado vortex moved over probes UF01 and UF07 at ~0005 UTC (UF01 and UF7 were collocated). Around that time only a few raindrops were observed with a small number concentration (<100 mm^{-1} m^{-3}) of small drops ($d < 1$ mm) with diameters < 1 mm and $Z <$ ~20 dBZ. Hardly any raindrops were observed at about 0006 UTC, which is related to the passage of the rain-free area of the hook appendage. This area of low reflectivity and hardly any raindrops is the updraft and inflow notch region of the supercell.

After 0005 UTC, the number concentration of medium- and large-size raindrops increased and graupel was observed more frequently. Only CU01 observed a few hailstones over several minutes (Fig. 5d). At all instruments, disdrometer-based Z, R, and w rapidly increased between 0005 and 0010 UTC (UF01, UF07) and 0007 and 0012 UTC (CU01), with Z ranging between 50 and 70 dBZ, R between 50 and 200 mm h^{-1}, and $w >$ 2 g m^{-3}. Although the number of larger particles increased, D_0 remained around 2 mm between 0005 and 0010 UTC (UF01, UF07), which is related to the increase in small-sized particles ($d < 2$ mm). Small-sized raindrops occurred when the wind speed and standard deviation of the wind speed increased between 0005 and 0010 UTC and around 0013 UTC, respectively (Fig. 13). The DSD gamma fit parameters from CU01 indicated brief increases in N_0, Λ, and μ at 0009 and 0013 UTC, supporting the increase in small-sized raindrops (Fig. 8b). Enhanced turbulence could be hypothesized to increase the number concentration of small drops between 0005 and 0008 UTC and 0011 and 0014 UTC (Fig. 13).

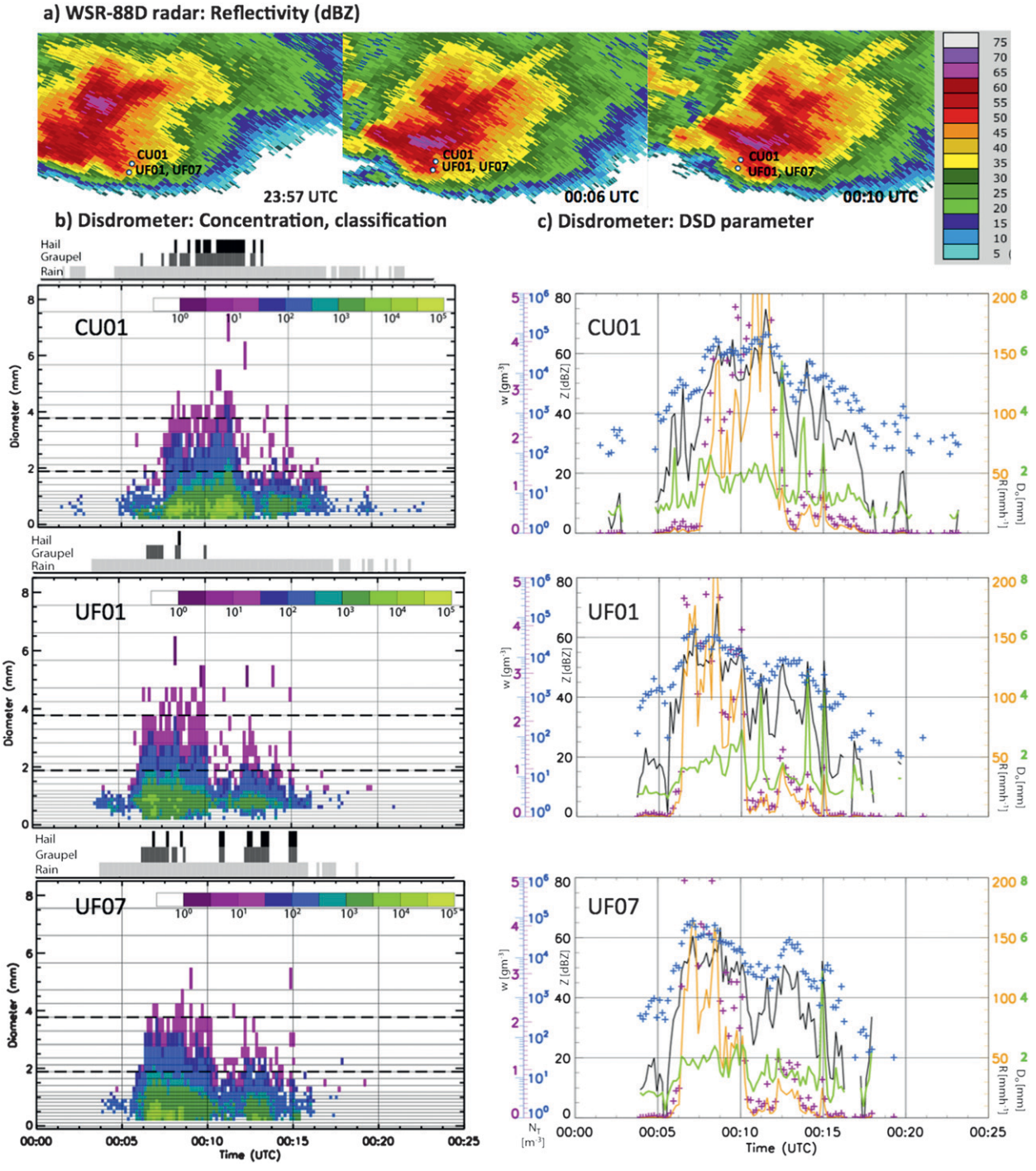

FIG. 11. As in Fig. 6, but for the first deployment on 7 Jun 2010 near Scottsbluff, NE. The articulating microphysical probe UF01 and the stationary probes CU01 and UF07 were deployed along a north–south road as indicated in (a) with probes UF01 and UF07 being collocated. WSR-88D radar reflectivity from Cheyenne, WY (KCYS), is also shown in (a). The distance between the storm and the radar was ~139 km; i.e., the radar beam was ~2.4 km above ground level.

The number concentration and N_T observed by CU01 increased around 0008 and 0011 UTC and increased at UF07 around 0006 UTC, when the wind speed was >15 m s^{-1} and the standard deviation of the wind speed was >2.5 m s^{-1}. During those times, the slope, shape, and intercept parameters observed by CU01 temporarily increased (Fig. 8b). All instruments observed a moderate number concentration of medium-sized particles and

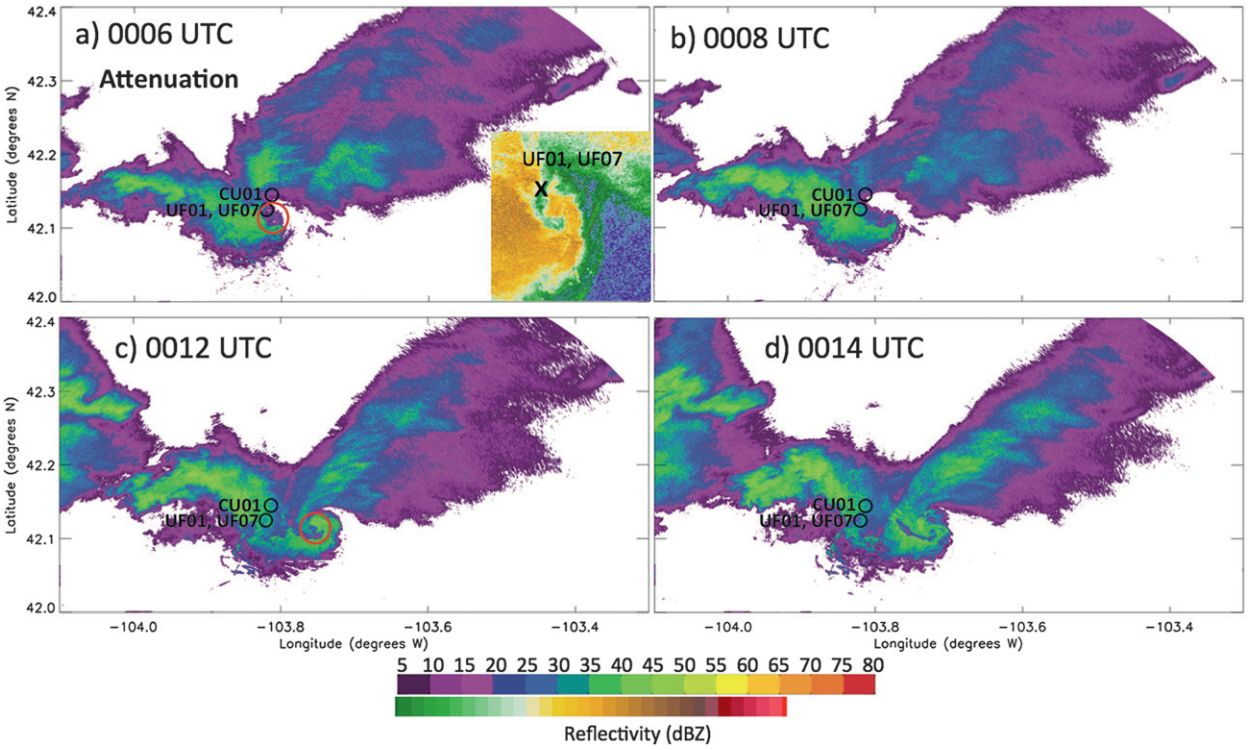

FIG. 12. As in Fig. 7, but for 7 Jun 2010. DOW6 was located ~6 km south of UF01. A tornado vortex signature was observed by DOW6 at 0006 and 0012 UTC; the location is indicated by the red circles in (a) and (c). A zoomed-in view of the reflectivity associated with the tornado at 3° elevation is shown in (a).

occasionally a large number concentration of large particles. At the edge of the storm (after 0011–0013 UTC), there was a rapid decrease in the number concentration, and the DSD parameters were characterized by large temporal variations. Disdrometer-based reflectivity values decreased to <50 dBZ, D_0 to 1.5 mm with occasional spikes of up to 5 mm, and w remained <2 g m^{-3}.

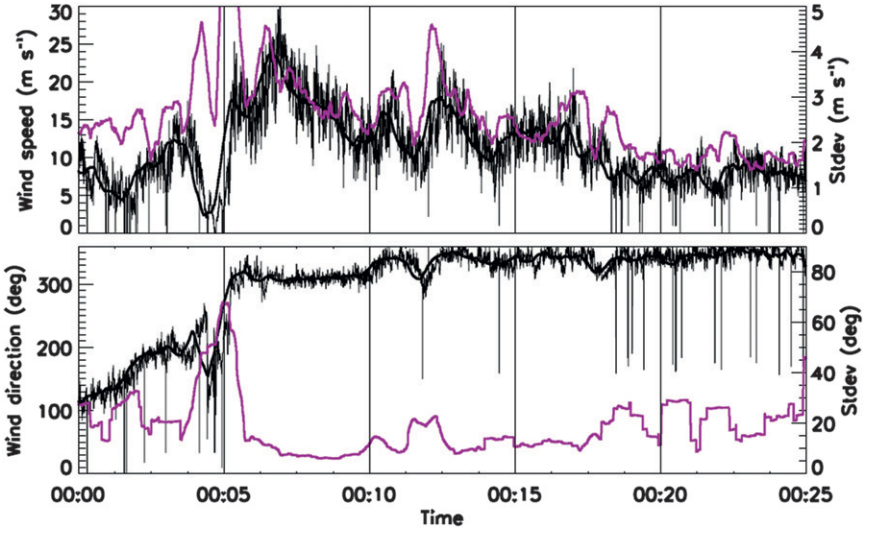

FIG. 13. Wind speed (top panel, thin black line) and direction (bottom panel, thin black line) measured at 17 Hz by UF01 on 7 Jun 2010. Wind averaged over 1 min (thick black lines in top and bottom panels) with standard deviations indicated as purple lines, respectively is also indicated.

5. Discussion

a. Hydrometeor size-sorting theory

Several studies hypothesize that size sorting of the hydrometeors occurs in convective storms in particular supercell thunderstorms. Vertical increase in wind velocity and the veering of the wind with height cause smaller hydrometers to be advected a considerable distance from the updraft, while larger raindrops and hail reach the surface close to the updraft due to their larger fall velocities (e.g., Browning and Donaldson 1963; Browning 1964, 1965; Hall et al. 1984; Ryzhkov et al. 2005; Tessendorf et al. 2005; Kumjian and Ryzhkov 2008, 2012; and references within). The thunderstorm observations on 18 May, 19 May, and 7 June were in large parts consistent with previous radar-based studies of size-sorting effects. Hail and graupel were mainly observed in the precipitation region close to the main updraft (CU01 on 18 May and 7 June) and only occasionally in the FFD and RFD close to the updraft (18 May). Although ice particles were observed, the accumulated number concentrations of ice particles were relatively low (Figs. 5b,d). While radar data within a few hundred meters of the surface have often captured hail close to the updraft region (e.g., Kumjian and Ryzhkov 2008), Morrison and Milbrandt (2011) showed that most of the graupel and hail in their supercell thunderstorm simulations melted before they reached the ground.

Rain was observed throughout the storm with larger raindrops occurring in the FFD close to the main updraft (18 May). Note that these large raindrops are likely part of the arc of large differential reflectivity Z_{dr} typically observed by dual-polarization radars along the right flank of the FFD (Kumjian and Ryzhkov 2008, 2009 and references within). Contrary to radar observations, the larger raindrops observed by the disdrometers were often accompanied by small raindrops, which could be formed from evaporation and breakup of larger drops, melting of small ice particles, and shedding of liquid water. Near-surface microphysical processes are usually not included in the size-sorting theory. Schuur et al. (2001) also observed an increase in the number of small drops ($d < 1$ mm) in the heavy precipitation area of a supercell thunderstorm. They also pointed out that raindrops of all sizes both abruptly increase and decrease, which has also been observed in this study. It should also be noted that radar parameters are dominated by larger drops and particles. Additionally, processes close to the surface are, for the most part, poorly captured by radars.

The measurements in the hook appendage on 7 June indicate the occurrence of hardly any large ice particles (i.e., hail) but showed small graupel and rain with medium-sized and small-sized drops (UF01 and UF07 on 7 June; Fig. 11). The passage of the tornado vortex signature was characterized by a small number concentration of small drops and a sudden increase in drop diameter once the vortex passed the instruments, with D_0 suddenly increasing from 1 to 4 mm and R reaching 100–200 mm h^{-1}.

b. Microphysical processes

Variability of rain and ice particles in supercell thunderstorms is strongly linked to a combination of microphysical, thermodynamic, and dynamical processes. While section 5a focused on dynamical processes, in this section we will discuss some possible microphysical processes. It should be noted that discussion about size-sorting and microphysical processes in this section and throughout the paper assumes a Lagrangian evolution of microphysical quantities versus drop size distribution evolution at a fixed point while the storm moves over the instruments. DSDs in convective storms are dominated by collection, melting of ice particles, evaporation, and breakup. Morrison and Milbrandt (2011) showed that the occurrence of a large number of small raindrops, which get evaporated more rapidly than larger raindrops, lead to stronger surface cold pools. Breakup of raindrops, identified in numerical models when the total number concentration increases and the mean-mass diameter decreases, was identified as a process that produces a large number of small raindrops in supercell thunderstorms (Morrison and Milbrandt 2011). As shown in section 5a, large-size raindrops occurred primarily close to the main updraft region together with ice particles, leading to the assumption that the large raindrops could originate from melting ice particles aloft. The number concentration of small-sized drops ($d < 2$ mm) constantly changes throughout the storms (section 4) but mainly increased in the area close to the updraft. On 18 May, the increase in smaller drops (from ~100 to ~10 000 mm^{-1} mm^{-3}) occurred between 2340 and 2345, 2355 and 0005, and 0011 and 0015 UTC (Figs. 6 and 8). Using a video disdrometer, Schuur et al. (2001) also observed an increase in smaller-sized drops in the area of heavy precipitation in supercell thunderstorms. On the other hand, radar analysis by Kumjian and Ryzhkov (2012) indicate that the size-sorting mechanism completely removes the small raindrops from the updraft region. The differences between disdrometer and radar observations could be due to processes (e.g., breakup) that occur close to the surface, which generally cannot be captured by radars or due to the limits of radar observations, which are dominated by large drops or particles. On 18 May, the mean diameter significantly decreased from 3 to 1.5 mm, while N_T increased during

2340–2345 UTC, which could be an indication of raindrop breakup. During the other times on 18 May (2355–0005 and 0011–0015 UTC), N_T and D_0 both remained constant or decreased. The large number of small raindrops could also be formed by the shedding of liquid water from hailstones (Rasmussen and Heymsfield 1987). Both processes could be supported by strong winds and turbulence at the surface (Figs. 6b and 12). Pruppacher and Klett (1997) and Tokay and Beard (1996) showed that turbulence only has an impact on large raindrop that reached the critical breakup size, which might occur in the boundary layer if wind speeds are >10 m s^{-1}. By analyzing wind profiler data, Kobayashi and Adachi (2001) observed the disappearance of giant raindrops ($\sim$6 mm) below 2.75 km above ground level and an increase in smaller raindrops ($<$1.5 mm) when the wind velocity was $\sim$10 m s^{-1}. They interpreted these variations as a result of raindrop breakup.

Collection and breakup processes in heavy rainfall rates are considered to be in balance (List and Gillespie 1976; Blanchard and Spencer 1970; Sekhon and Srivastava 1971; Pasqualucci 1982; Hodson 1986; Hu and Srivastava 1995). However, several other studies found that the slope of the DSD decreases with increasing rainfall rate in areas of moderate rainfall, an indication that processes are not in balance (Shiotsuki 1976; Zawadzki and de Agostinho Antonio 1988; Willis and Tattelman 1989; Sauvageot and Lacaux 1995). Obviously, answering the question of equilibrium between collection and breakup is beyond the scope of this paper. However, we will discuss the temporal variation of the DSD parameters, in particular the temporal evolution of the slope Λ and intercept N_0 parameter as a function of rainfall rate. During heavy rainfall ($>$40 mm h^{-1}) on 18 May and 7 June (indicated by arrows in Fig. 8), N_0 increased. Increases in the intercept parameter N_0 have often been observed in convective storms, especially when transitioning between the convective and stratiform regions of the storm, where aggregation of ice particles and subsequent melting into stratiform rain were dominant processes (Waldvogel 1974; Donnadieu 1982; Tokay and Short 1996; Uijlenhoet et al. 2003b). Uijlenhoet et al. (2003a) and Steiner et al. (2004) argue that the changes in DSD in extreme rainfall ($R > 100$ mm h^{-1}) are related to varying raindrop concentrations, while collection and breakup are still in equilibrium. Only on 18 May at 2340–2345 and 2355–0000 UTC did the slope parameter remain mainly constant (i.e., collection and breakup could be in balance), while Λ varied during all other times. We can assume that during those times (2340–2345 and 2355–0000 UTC 18 May) collection and breakup were in balance. Hu and Srivastava (1995) pointed out that the DSD is not in equilibrium if evaporation is included.

6. Conclusions

We examined the use of mobile disdrometers for the collection of in situ microphysical data in severe thunderstorms during VORTEX2 and demonstrated that the deployment of mobile and rapidly deployable PARSIVEL disdrometers is suitable for the collection of in situ microphysical data within severe thunderstorms. The study focuses on analyzing the variability of DSDs and DSD parameters in various regions of a supercell thunderstorm and two merging convective cells and relates the results to size-sorting theory and microphysical processes.

The use of portable microphysical probes enabled us to place the instruments in the path of the supercell thunderstorms and in the areas of greatest interest. Two deployment strategies truck and unmanned, and two instrument types, articulating and stationary disdrometers, were used during VORTEX2 during 2009 and 2010. Since instruments can be redeployed quickly, the truck deployment was chosen in nonsevere conditions. The unmanned deployment was preferable in severe conditions with large hail and tornadoes. While articulating and stationary disdrometers show a similar level of performance, the articulating disdrometers were especially useful during strong winds, when stationary PARSIVEL disdrometers misclassified some of the observed particles (FHML).

The selected case studies showed the ability of the in situ observations to study size-sorting theory and microphysical processes. Hailstones, graupel, and large raindrops were primarily observed close to the updraft region of the storm in the FFD and RFD. The supercell thunderstorms presented in this study had rainfall rates close to the updraft $>$70–100 mm h^{-1}, w ranging between 2 and 5 g m^{-3}, and D_0 of 2–3 mm. Toward the edges of the thunderstorm, fewer graupel and hailstones as well as small- and medium-sized raindrops were observed. The merging thunderstorms had on average smaller particles compared to the supercell thunderstorms. Interestingly, the edge of those storms showed a clear separation between medium-size particles at the edge of the storm with a lack of small-size particles and an increased number of small-size particles in the center of the storm.

The observations on 18 May, 19 May, and 7 June were consistent in large part with previous studies of size-sorting effects. Hail and graupel were mainly observed in the precipitation region close to the main updraft and only occasionally in the FFD and RFD close to the updraft. The larger raindrops observed by the disdrometers close to the updraft were often accompanied by small raindrops. Large temporal variations in the DSD were

observed in all three examples. Contrary to radar observations, the larger raindrops observed by the disdrometers were often accompanied by small raindrops, which could be formed from evaporation and breakup of larger drops, melting of small ice particles, and shedding of liquid water. An increase in small-size drops was observed when the wind speed and standard deviation of the wind speed increased, which can be hypothesized to be related to raindrop breakup processes. Observations also indicate an increase in the slope and intercept parameters when the number of small-size drops increased. It can be hypothesized that the DSD undergoes large variations related to the melting of ice particles, raindrop breakup, and evaporation, as well as dynamic and thermodynamic processes. In all cases except on 18 May at ~0000 UTC the variations in the DSD are collocated with changes in the total number concentrations. Although Uijlenhoet et al. (2003a) and Steiner et al. (2004) argue that the changes in DSD can be related to raindrop concentration with breakup and collection being in equilibrium, we believe that the combination of thermodynamic, dynamic, and microphysical processes might change the DSD.

Gamma functional fit parameters and DSD observed during VORTEX2 generally resemble those observed by Schuur et al. (2001) using a video disdrometer in a supercell thunderstorm. Total number concentration (1000–50 000 m^{-3}) and mean diameter (1–3 mm) in supercell thunderstorm and convective cells are much higher than those observed in stratiform rain. Cao et al. (2008) analyzed rain in Oklahoma between 2005 and 2007 with a video disdrometer. Their average total number concentration ranged between 500 and 3000 m^{-3} and the mean diameter between 1 and 2.5 mm. The large variability of those parameters makes it difficult to assume fixed parameters in microphysical parameterization schemes. For example, one-moment microphysics parameterizations typically assume an exponential DSD with a constant N_0 equal to 10^7 m^{-4} (Dudhia 1989; Grabowski 1998) or 8×10^6 m^{-4} (Lin et al. 1983; Rutledge and Hobbs 1984; Reisner et al. 1998; Thompson et al. 2008). The observations in supercell thunderstorms and the convective cells show large variations in N_0 assuming a gamma DSD ranging between 10^3 and 10^5 $mm^{-1-\mu}$ m^{-3}. Large variations were also observed in the mean diameter. While for most of the time D_0 ranged around 2 mm, it reached up to 6 mm for short time periods.

What are the microphysical and dynamic conditions that might produce these modes in the DSD? Can we observe these modes in other parts of thunderstorms? Answering these questions requires the analysis of thermodynamic and dynamic fields as well as a larger dataset of disdrometer observations, which is beyond the scope of this paper but will be addressed in the future. With the VORTEX2 disdrometer dataset we are able to explore temporal and spatial variations of DSD in different areas of the storm and at different stages. The results can be used to better understand the microphysical processes that occur in thunderstorms and can be applied to cloud model simulations. The coupling of disdrometer measurements with observations from mobile polarimetric Doppler radars and surface stations may provide an opportunity to gain a deeper understanding of the relationship between the three-dimensional microphysics, thermodynamics, and dynamics of the supercell and its DSD.

Acknowledgments. We extend special thanks to Rachel Humphrey, Danielle Nuding, Stephanie Higgins, George Fernandez, Scott Landolt, and Cameron Redwine, who helped deploy the disdrometers during the VORTEX2 field campaign. We thank Scott Kittelman of the University of Colorado for helping prepare the instruments used on VORTEX2. The authors thank Joshua Wurman and Karen Kosiba of the Center for Severe Weather Research (CSWR) and Donald Burgess of the Cooperative Institute for Mesoscale Meteorological Studies (CIMMS), University of Oklahoma, Norman, Oklahoma, for providing radar data and information on the tornado vortex signatures for the cases discussed in this paper. The authors thank the two anonymous reviewers for their assistance in evaluating this paper. This research was sponsored by the National Science Foundation under Grants ATM 0910424 (Friedrich) and AGS 0969172 (Friedrich). Any opinions, findings, and conclusions or recommendations expressed in this paper are those of the authors and do not necessarily reflect the views of the sponsors, partners and contributors.

APPENDIX

Description of the Moments of the DSD and Gamma Functional Fit

The number concentrations for each hydrometeor type were summed over all of the velocity classes using the measured average fall velocity per diameter class to determine $N(D)_i$ to calculate moments of the drop-size distribution such as reflectivity Z, rainfall rate R, liquid water content w, and median-volume diameter D_0 at a temporal resolution of 10 s, following Ulbrich (1983), Testud et al. (2001), Bringi et al. (2003), and Yuter et al. (2006) and references within:

$$Z(\mathrm{dB}Z) = 10 \log_{10} \sum_i N(D)_i D_i^6 \Delta D_i, \qquad \text{(A1)}$$

$$R(\text{mm h}^{-1}) = 3.6 \times 10^{-3} \frac{\pi}{6} \sum_i N(D)_i D_i^3 V(D)_i \Delta D_i, \quad \text{and} \tag{A2}$$

$$w(\text{g m}^{-3}) = 10^{-9} \rho_w \frac{\pi}{6} \sum_i N(D)_i D_i^3 \Delta D_i, \tag{A3}$$

where ρ_w is the particle density ($\rho_w = 10^6$ g m^{-3} for rain). The median-volume diameter, D_0, was derived by accumulating the drop volume measured by the disdrometer and then taking the drop diameter with the same total accumulated volume in two equal parts: $2\sum_{D_{\min}}^{D_0} D^3 N(D)_i \Delta D_i = \sum_{D_{\min}}^{D_{\max}} D^3 N(D)_i \Delta D_i$. Even though PSDs from hail and graupel were observed, the analysis was limited to raindrop-size distributions.

The data sampled over 10 s varies significantly due to the variability of rain in general and variations in the dynamic and thermodynamic conditions of the environment. Most studies average the number concentration over 1 min, which relates to a horizontal displacement of rain comparable to the mean size of a radar volume. To compare our results to other studies, the normalized number concentration within each diameter class averaged over 1 min was used to apply a theoretical gamma distribution fit. Additionally, only time steps when the rainfall rate exceeded 5 mm h^{-1} and the total drop count was larger than 1000 (Zhang et al. 2003) were used.

The gamma function $N(D) = N_0 D^{\mu} \exp(-\Lambda D)$ is used to represent the DSD in rain (Ulbrich 1983). The DSD function parameters [i.e., the shape (μ unitless), slope (Λ in mm^{-1}), and intercept (N_0 in mm$^{-1-\mu}$ m^{-3}) parameters] are derived from the second, fourth, and sixth moments (M_2, M_4, and M_6), respectively, according to Zhang et al. (2003) and Moisseev and Chandrasekar (2007). The parameters can be estimated from

$$N_0 = \frac{M_2 \Lambda^{\mu+3}}{\Gamma(\mu+3)}, \tag{A4}$$

$$\Lambda = \left[\frac{M_2 \Gamma(\mu+5)}{M_4 \Gamma(\mu+3)}\right]^{1/2}, \quad \text{and} \tag{A5}$$

$$\mu = \frac{(7-11\eta) - (\eta^2 + 14\eta + 1)^{1/2}}{2(\eta - 1)}, \quad \text{with} \quad \eta = \frac{M_4^2}{M_6 M_2}. \tag{A6}$$

For more information, the reader is referred to Zhang et al. (2003) and Moisseev and Chandrasekar (2007). Note that small drops can be deflected before they enter the sampling area under strong wind conditions, resulting in an underestimation of smaller drops (Nespor et al. 2000). While small-size raindrops have lower impact on the higher-order moments of the DSD (e.g., reflectivity), lower-order moments (e.g., median volume diameter) and the gamma functional fit will be affected by the undersampling of small drops.

REFERENCES

Atlas, D., R. C. Srivastava, and R. S. Sekhon, 1973: Doppler radar characteristics of precipitation at vertical incidence. *Rev. Geophys.,* **11,** 1–35.

Barthazy, E., S. Goeke, R. Schefold, and D. Hoegl, 2004: An optical array instrument for shape and fall velocity measurements of hydrometeors. *J. Atmos. Oceanic Technol.,* **21,** 333–344.

Battaglia, A., E. Rustemeier, A. Tokay, U. Blahak, and C. Simmer, 2010: PARSIVEL snow observations: A critical assessment. *J. Atmos. Oceanic Technol.,* **27,** 1400–1416.

Blanchard, D. C., and A. T. Spencer, 1970: Experiments on the generation of raindrop-size distributions by drop breakup. *J. Atmos. Sci.,* **27,** 101–108.

Bluestein, H. B., M. M. French, R. L. Tanamachi, S. Frasier, K. Hardwick, F. Junyent, and A. L. Pazmany, 2007: Close-range observations of tornadoes in supercells made with a dual-polarization, X-band, mobile Doppler radar. *Mon. Wea. Rev.,* **135,** 1522–1543.

Bradley, S. G., and C. D. Stow, 1975: Reply. *J. Appl. Meteor.,* **14,** 426–428.

Brandes, E. A., J. Vivekanandan, J. D. Tuttle, and C. J. Kessinger, 1995: A study of thunderstorm microphysics with multiparameter radar and aircraft observations. *Mon. Wea. Rev.,* **123,** 3129–3143.

Bringi, V. N., D. A. Burrows, and S. M. Menon, 1991: Multiparameter radar and aircraft study of raindrop spectral evolution in warm-based clouds. *J. Appl. Meteor.,* **30,** 853–880.

——, L. Liu, P. C. Kennedy, V. Chandrasekar, and S. A. Rutledge, 1996: Dual multiparameter radar observations of intense convective storms: The 24 June 1992 case study. *Meteor. Atmos. Phys.,* **59,** 3–31.

——, V. Chandrasekar, J. Hubbert, E. Gorgucci, W. L. Randeu, and M. Schoenhuber, 2003: Raindrop size distribution in different climatic regimes from disdrometer and dual-polarized radar analysis. *J. Atmos. Sci.,* **60,** 354–365.

Browning, K. A., 1964: Airflow and precipitation trajectories within severe local storms which travel to the right of the winds. *J. Atmos. Sci.,* **21,** 634–639.

——, 1965: The evolution of tornadic storms. *J. Atmos. Sci.,* **22,** 664–668.

——, and R. J. Donaldson Jr., 1963: Airflow and structure of a tornadic storm. *J. Atmos. Sci.,* **20,** 533–545.

Burgess, D. W., M. A. Magsig, J. Wurman, D. C. Dowell, and Y. Richardson, 2002: Radar observations of the 3 May 1999 Oklahoma City tornado. *Wea. Forecasting,* **17,** 456–471.

Cao, Q., G. Zhang, E. Brandes, T. Schuur, A. Ryzhkov, and K. Ikeda, 2008: Analysis of video disdrometer and polarimetric radar data to characterize rain microphysics in Oklahoma. *J. Appl. Meteor. Climatol.,* **47,** 2238–2255.

Caracciolo, C., F. Rodi, and R. Uijlenhoet, 2006: Comparison between Pludix and impact/optical disdrometers during rainfall measurement campaigns. *Atmos. Res.,* **82,** 137–163.

Donnadieu, G., 1982: Observation de deux changements des spectres des gouttes de pluie dans une averse de nuages stratiformes. *J. Rech. Atmos.,* **16,** 35–45.

Dudhia, J., 1989: Numerical study of convection observed during the Winter Monsoon Experiment using a mesoscale two-dimensional model. *J. Atmos. Sci.,* **46,** 3077–3107.

Ferrier, B. S., W.-K. Tao, and J. Simpson, 1995: A double-moment multiple-phase four-class bulk ice scheme. Part II: Simulations of convective storms in different large-scale environments and comparisons with other bulk parameterizations. *J. Atmos. Sci.,* **52,** 1001–1033.

Fovell, R. G., and Y. Ogura, 1988: Numerical simulation of a midlatitude squall line in two dimensions. *J. Atmos. Sci.,* **45,** 3846–3879.

Gilmore, M. S., J. M. Straka, and E. N. Rasmussen, 2004: Precipitation uncertainty due to variations in precipitation particle parameters within a simple microphysics scheme. *Mon. Wea. Rev.,* **132,** 2610–2627.

Grabowski, W. W., 1998: Toward cloud resolving modeling of large-scale tropical circulations: A simple cloud microphysics parameterization. *J. Atmos. Sci.,* **55,** 3283–3298.

Griffiths, R. F., 1975: Comments on ''The measurement of charge and size of raindrops: Parts I and II.'' *J. Appl. Meteor.,* **14,** 422–425.

Grzych, M. L., B. D. Lee, and C. A. Finley, 2007: Thermodynamic analysis of supercell rear-flank downdrafts from Project ANSWERS. *Mon. Wea. Rev.,* **135,** 240–246.

Gunn, R., and G. D. Kinzer, 1949: The terminal velocity of fall for water droplets in stagnant air. *J. Meteor.,* **6,** 243–248.

Hall, M. P. M., J. W. F. Goddard, and S. M. Cherry, 1984: Identification of hydrometeors and other targets by dual-polarization radar. *Radio Sci.,* **19,** 132–140.

Hodson, M. C., 1986: Raindrop size distribution. *J. Climate Appl. Meteor.,* **25,** 1070–1074.

Hu, Z., and R. C. Srivastava, 1995: Evolution of raindrop size distribution by coalescence, breakup, and evaporation: Theory and observations. *J. Atmos. Sci.,* **52,** 1761–1783.

Hubbert, J., V. N. Bringi, L. D. Carey, and S. Bolen, 1998: CSU-CHILL polarimetric measurements from a severe hailstorm in eastern Colorado. *J. Appl. Meteor.,* **37,** 749–755.

Huschke, R. E., 1959: *Glossary of Meteorology.* Amer. Meteor. Soc., 638 pp.

Illingworth, A. J., and C. J. Stevens, 1987: An optical disdrometer for the measurement of raindrop size spectra in windy conditions. *J. Atmos. Oceanic Technol.,* **4,** 411–421.

Jaffrain, J., and A. Berne, 2011: Experimental quantification of the sampling uncertainty associated with measurements from PARSIVEL disdrometers. *J. Hydrometeor.,* **12,** 352–370.

Kennedy, P. C., and S. A. Rutledge, 1995: Dual-Doppler and multiparameter radar observations of a bow-echo hailstorm. *Mon. Wea. Rev.,* **123,** 921–943.

Knight, N. C., 1983: Measurement and interpretation of hailstone density and terminal velocity. *J. Atmos. Sci.,* **40,** 1510–1516.

Kobayashi, T., and A. Adachi, 2001: Measurements of raindrop breakup by using UHF wind profilers. *Geophys. Res. Lett.,* **28,** 4071–4074.

Krajewski, W. F., and Coauthors, 2006: DEVEX—Disdrometer Evaluation Experiment: Basic results and implications for hydrologic studies. *Adv. Water Resour.,* **29,** 311–325.

Kruger, A., and W. F. Krajewski, 2002: Two-dimensional video disdrometer: A description. *J. Atmos. Oceanic Technol.,* **19,** 602–617.

Kumjian, M. R., and A. V. Ryzhkov, 2008: Polarimetric signatures in supercell thunderstorms. *J. Appl. Meteor. Climatol.,* **47,** 1940–1961.

——, and ——, 2009: Storm-relative helicity revealed from polarimetric radar measurements. *J. Atmos. Sci.,* **66,** 667–685.

——, and ——, 2012: The impact of size sorting on the polarimetric radar variables. *J. Atmos. Sci.,* **69,** 2042–2060.

Lin, Y.-L., R. D. Farley, and H. D. Orville, 1983: Bulk parameterization of the snow field in a cloud model. *J. Climate Appl. Meteor.,* **22,** 1065–1092.

List, R., and J. R. Gillespie, 1976: Evolution of raindrop spectra with collision-induced breakup. *J. Atmos. Sci.,* **33,** 2007–2013.

Liu, C., M. W. Moncrieff, and E. J. Zipser, 1997: Dynamical influence of microphysics in tropical squall lines: A numerical study. *Mon. Wea. Rev.,* **125,** 2193–2210.

Locatelli, J. D., and P. V. Hobbs, 1974: Fall speeds and masses of solid precipitation particles. *J. Geophys. Res.,* **79,** 2185–2197.

Loeffler-Mang, M., and J. Joss, 2000: An optical disdrometer for measuring size and velocity of hydrometeors. *J. Atmos. Oceanic Technol.,* **17,** 130–139.

——, and U. Blahak, 2001: Estimation of the equivalent radar reflectivity factor from measured snow size spectra. *J. Appl. Meteor.,* **40,** 843–849.

Loney, M. L., D. S. Zrnić, J. M. Straka, and A. V. Ryzhkov, 2002: Enhanced polarimetric radar signatures above the melting level in a supercell storm. *J. Appl. Meteor.,* **41,** 1179–1194.

Lopez, C. R., F. J. Masters, and K. Friedrich, 2011: Capture and characterization of wind-driven rain during tropical cyclones and supercell thunderstorms. *13th Int. Conf. on Wind Engineering,* Amsterdam, The Netherlands, International Association for Wind Engineering.

Lord, S. J., H. E. Willoughby, and J. M. Piotrowicz, 1984: Role of a parameterized ice-phase microphysics in an axisymmetric, nonhydrostatic tropical cyclone model. *J. Atmos. Sci.,* **41,** 2836–2848.

Markowski, P., J. M. Straka, and E. N. Rasmussen, 2002: Direct surface thermodynamic observations within the rear-flank downdrafts of nontornadic and tornadic supercells. *Mon. Wea. Rev.,* **130,** 1692–1721.

——, and Coauthors, 2012: The pretornadic phase of the Goshen County, Wyoming, supercell of 5 June 2009 intercepted by VORTEX2. Part I: Evolution of kinematic and surface thermodynamic fields. *Mon. Wea. Rev.,* **140,** 2887–2915.

McCumber, M., W.-K. Tao, J. Simpson, R. Penc, and S.-T. Soong, 1991: Comparison of ice-phase microphysical parameterization schemes using numerical simulations of tropical convection. *J. Appl. Meteor.,* **30,** 985–1004.

Moisseev, D. N., and V. Chandrasekar, 2007: Examination of the μ–Λ relation suggested for drop size distribution parameters. *J. Atmos. Oceanic Technol.,* **24,** 847–855.

Morrison, H., and J. Milbrandt, 2011: Comparison of two-moment bulk microphysics schemes in idealized supercell thunderstorm simulations. *Mon. Wea. Rev.,* **139,** 1103–1130.

——, G. Thompson, and V. Tatarskii, 2009: Impact of cloud microphysics on the development of trailing stratiform precipitation in a simulated squall line: Comparison of one- and two-moment schemes. *Mon. Wea. Rev.,* **137,** 991–1007.

Musil, D. J., W. R. Sand, and R. A. Schleusener, 1973: Analysis of data from T-28 aircraft penetrations of a Colorado hailstorm. *J. Appl. Meteor.,* **12,** 1364–1370.

Nespor, V., W. F. Krajewski, and A. Kruger, 2000: Wind-induced error of raindrop size distribution measurement using a two-dimensional video disdrometer. *J. Atmos. Oceanic Technol.,* **17,** 1483–1492.

Pasqualucci, F., 1982: The variation in drop size distribution in convective storms: A comparison between theory and measurement. *Geophys. Res. Lett.,* **9,** 839–841.

Pruppacher, H. R., and J. D. Klett, 1997: *Microphysics of Clouds and Precipitation.* Kluwer Academic, 954 pp.

Rasmussen, R. M., and A. J. Heymsfield, 1987: Melting and shedding of graupel and hail. Part I: Model physics. *J. Atmos. Sci.,* **44,** 2754–2763.

Rauber, R. M., K. V. Beard, and B. M. Andrews, 1991: A mechanism for giant raindrop formation in warm, shallow convective clouds. *J. Atmos. Sci.,* **48,** 1791–1797.

Reisner, J., R. M. Rasmussen, and R. T. Bruintjes, 1998: Explicit forecasting of supercooled liquid water in winter storms using the MM5 mesoscale model. *Quart. J. Roy. Meteor. Soc.,* **124,** 1071–1107.

Romine, G. S., D. W. Burgess, and R. B. Wilhelmson, 2008: A dual-polarization-radar-based assessment of the 8 May 2003 Oklahoma City area tornadic supercell. *Mon. Wea. Rev.,* **136,** 2849–2870.

Rutledge, S. A., and P. V. Hobbs, 1984: The mesoscale and microscale structure and organization of clouds and precipitation in midlatitude cyclones. XII: A diagnostic modeling study of precipitation development in narrow cold-frontal rainbands. *J. Atmos. Sci.,* **41,** 2949–2972.

Ryzhkov, A. V., T. J. Schuur, D. W. Burgess, and D. S. Zrnić, 2005: Polarimetric tornado detection. *J. Appl. Meteor.,* **44,** 557–570.

Sauvageot, H., and J.-P. Lacaux, 1995: The shape of averaged drop size distributions. *J. Atmos. Sci.,* **52,** 1070–1083.

Schlatter, P. T., 2003: Polarimetric radar and in-situ measurements of a nontornadic supercell. M.S. thesis, School of Meteorology, University of Oklahoma, 97 pp.

Schuur, T. J., A. V. Ryzhkov, D. S. Zrnic, and M. Schoenhuber, 2001: Drop size distributions measured by a 2D video disdrometer: Comparison with dual-polarization radar data. *J. Appl. Meteor.,* **40,** 1019–1034.

Sekhon, R. S., and R. C. Srivastava, 1971: Doppler radar observations of drop-size distributions in a thunderstorm. *J. Atmos. Sci.,* **28,** 983–994.

Sevruk, B., 1982: Methods of correction for systematic error in point precipitation measurement for operational use. Operational Hydrological Rep. 21, WMO Rep. 589, 91 pp.

Shabbott, C. J., and P. M. Markowski, 2006: Surface in situ observations within the outflow of forward-flank downdrafts of supercell thunderstorms. *Mon. Wea. Rev.,* **134,** 1422–1441.

Shiotsuki, Y., 1976: An estimation of drop-size distribution in the severe rainfall. *J. Meteor. Soc. Japan,* **54,** 259–263.

Smyth, T. J., and A. J. Illingworth, 1998: Correction for attenuation of radar reflectivity using polarization data. *Quart. J. Roy. Meteor. Soc.,* **124,** 2393–2415.

Steiner, M., J. A. Smith, and R. Uilenhoet, 2004: A microphysical interpretation of radar reflectivity–rain rate relationships. *J. Atmos. Sci.,* **61,** 1114–1131.

Szumowski, M. J., R. M. Rauber, H. T. Ochs, and K. V. Beard, 1998: The microphysical structure and evolution of Hawaiian rainband clouds. Part II: Aircraft measurements within rainbands containing high reflectivity cores. *J. Atmos. Sci.,* **55,** 208–226.

Tessendorf, S. A., L. J. Miller, K. C. Wiens, and S. A. Ruthledge, 2005: The 29 June 2000 supercell observed during STEPS. Part I: Kinematics and microphysics. *J. Atmos. Sci.,* **62,** 4127–4150.

Testud, J., S. Oury, R. A. Black, P. Amayenc, and X. Dou, 2001: The concept of ''normalized'' distribution to describe raindrop spectra: A tool for cloud physics and cloud remote sensing. *J. Appl. Meteor.,* **40,** 1118–1140.

Thompson, G., P. R. Field, R. M. Rasmussen, and W. D. Hall, 2008: Explicit forecasts of winter precipitation using an improved bulk microphysics scheme. Part II: Implementation of a new snow parameterization. *Mon. Wea. Rev.,* **136,** 5095–5115.

Thurai, M., and V. N. Bringi, 2005: Drop axis ratios from a 2D video disdrometer. *J. Atmos. Oceanic Technol.,* **22,** 966–978.

——, ——, and P. T. May, 2010a: CPOL radar-derived drop size distribution statistics of stratiform and convective rain for two regimes in Darwin, Australia. *J. Atmos. Oceanic Technol.,* **27,** 932–942.

——, W. A. Petersen, and L. D. Carey, 2010b: DSD characteristics of cool-season tornadic storm using C-band polarimetric radar and two 2D-video disdrometers. *Proc. Sixth Conf. on Radar in Meteorology and Hydrology,* Sibiu, Romania, EUMETSAT. [Available online at http://www.erad2010.org/pdf/oral/tuesday/radpol1/5_ERAD2010_0101.pdf.]

——, ——, A. Tokay, C. Schultz, and P. Gatlin, 2011: Drop size distribution comparisons between PARSIVEL and 2-D video disdrometers. *Adv. Geosci.,* **30,** 3–9.

Tokay, A., and K. V. Beard, 1996: A field study of raindrop oscillations. Part I: Observation of size spectra and evaluation of oscillation causes. *J. Appl. Meteor.,* **35,** 1671–1687.

——, and D. A. Short, 1996: Evidence from tropical raindrop spectra of the origin of rain from stratiform versus convective clouds. *J. Appl. Meteor.,* **35,** 355–371.

——, A. Kruger, and W. F. Krajewski, 2001: Comparison of drop size distribution measurements by impact and optical disdrometers. *J. Appl. Meteor.,* **40,** 2083–2097.

Uijlenhoet, R., J. A. Smith, and M. Steiner, 2003a: The microphysical structure of extreme precipitation as inferred from ground-based raindrop spectra. *J. Atmos. Sci.,* **60,** 1220–1238.

——, M. Steiner, and J. A. Smith, 2003b: Variability of raindrop size distributions in a squall line and implications for radar rainfall estimation. *J. Hydrometeor.,* **4,** 43–61.

Ulbrich, C. W., 1983: Natural variations in the analytical form of the raindrop size distribution. *J. Climate Appl. Meteor.,* **22,** 1764–1775.

Van Den Broeke, M. S., J. M. Straka, and E. N. Rasmussen, 2008: Polarimetric radar observations at low levels during tornado life cycles in a small sample of classic Southern Plains supercells. *J. Appl. Meteor. Climatol.,* **47,** 1232–1247.

Waldvogel, A., 1974: The N_0 jump of raindrop spectra. *J. Atmos. Sci.,* **31,** 1067–1078.

Willis, P. T., and P. Tattelman, 1989: Drop-size distributions associated with intense rainfall. *J. Appl. Meteor.,* **28,** 3–15.

Wurman, J., and S. Gill, 2000: Finescale radar observations of the Dimmitt, Texas (2 June 1995), tornado. *Mon. Wea. Rev.,* **128,** 2135–2164.

——, Y. Richardson, C. Alexander, S. Weygandt, and P. F. Zhang, 2007: Dual-Doppler analysis of winds and vorticity budget terms near a tornado. *Mon. Wea. Rev.,* **135,** 2392–2405.

——, K. Kosiba, P. Markowski, Y. Richardson, D. Dowell, and P. Robinson, 2010: Finescale single- and dual-Doppler analysis of tornado intensification, maintenance, and dissipation in the Orleans, Nebraska, supercell. *Mon. Wea. Rev.,* **138,** 4439–4455.

——, D. Dowell, Y. Richardson, P. Markowski, E. Rasmussen, D. Burgess, L. Wicker, and H. Bluestein, 2012: The second Verification of the Origins of Rotation in Tornadoes Experiment: VORTEX2. *Bull. Amer. Meteor. Soc.,* **93,** 1147–1170.

Yuter, S. E., D. E. Kingsmill, L. B. Nance, and M. Loeffler-Mang, 2006: Observations of precipitation size and fall speed characteristics within coexisting rain and wet snow. *J. Appl. Meteor. Climatol.,* **45,** 1450–1464.

Zawadzki, I., and M. de Agostinho Antonio, 1988: Equilibrium raindrop size distributions in tropical rain. *J. Atmos. Sci.,* **45,** 3452–3459.

Zhang, G. F., J. Vivekanandan, E. A. Brandes, R. Meneghini, and T. Kozu, 2003: The shape–slope relation in observed gamma raindrop size distributions: Statistical error or useful information? *J. Atmos. Oceanic Technol.,* **20,** 1106–1119.